This article has been accepted for publication in a future issue of this journal, but has not been fully edited. Content may change prior to final publication. Citation information: DOI 10.1109/ACCESS.2021.3072899, IEEE Access

IEEE Access
Multidisciplinary | Rapid Review | Open Access Journal

Date of publication xxxx 00, 0000, date of current version xxxx 00, 0000.

Digital Object Identifier 10.1109/ACCESS.2021.Doi Number

Design Implementation and Operation of an Education Laboratory-Scale Microgrid

Alper Nabi Akpolat[1], (Student Member, IEEE), Yongheng Yang[2], (Senior Member, IEEE), Frede Blaabjerg[3], (Fellow, IEEE), Erkan Dursun[1], (Member, IEEE) and Ahmet Emin Kuzucuoğlu[1], (Member, IEEE)

[1]Department of Electrical-Electronics Engineering, Faculty of Technology, Marmara University, Istanbul, 34722, Turkey
[2]College of Electrical Engineering, Zhejiang University, Hangzhou 310027, China
[3]Department of Energy Technology, Aalborg University, Aalborg, 9220, Denmark

Corresponding author: Alper Nabi Akpolat (e-mail: alper.nabi@marmara.edu.tr)

"This work was supported in part by Marmara University-BAPKO with FEN-C-DRP-150218-0063 project number and YUDAB program scholarship commission by The Council of Higher Education (YÖK)."

ABSTRACT To enable more wide-scale exploitation of renewable energy sources (RESs), distributed generations (DGs) as in microgrids have gained prominence recently. This study describes the design, modeling, implementation, and operation of a microgrid, in which a standalone hybrid power system has been installed for an education and research laboratory. The unstable nature of RESs results in power compatibility issues on DGs. Therefore, providing a decent power flow from renewables to loads is the scope of this paper. To satisfy defined load profiles and sustain the power with the desired level, the design and operation of power converters are a remarkable part of performing microgrids as well. For a robust microgrid structure, the presented control algorithm includes an energy management system (EMS) between renewables, batteries, and loads. Primarily, modeling of the system has been developed in MATLAB/Simulink environment. Additionally, case studies have been exemplified to further demonstrate the simulated system. Within this scope, certain load profiles not only have been fed but also power flow has been managed and analyzed to ensure effective and flexible operation with two different EMS cases. The real-time operation has been also provided to validate the system under various input and output conditions during a lab course.

INDEX TERMS Education laboratory, energy management system, distributed generation, microgrid, power electronic converters, renewable energy sources.

I. INTRODUCTION

For the last century, global warming has reached a remarkable stage rapidly due to CO_2 emission. In the near future, stepping to renewable energy sources (RESs) such as hydraulic, wind, solar, hydrogen, wave, geothermal, and biomass energy is expected to accelerate fast. Microgrids refer to the integration of distributed generation (DG) with high penetration of renewable resources.

Another emerging definition about microgrids is that they are a part of smart grids which increases the supply flexibility of smart grids. A microgrid can be described as a part of power grid with DG based on renewable sources, power electronics converters, energy storage systems, and loads, which can run standalone, and also interact with the utility grid [1]. The transformation of the existing energy into technology, production, transmission, distribution, and control also causes many challenges. DGs are expected to produce a smooth power, but it is not an effortless transaction due to their intermittent physical inputs [2]. To this end, robust and sophisticated control algorithms-aided stable microgrid applications are essential with help of robust operation of power electronic interfaces and energy management requirements [3]. Because of these unbalanced physical factors, to obtain maximum power as much as the system can, they are not preferred to operate without any converters which have control algorithms. In these topologies, the power electronics converters play a crucial role in dispatching stable power [4]. Briefly, providing robust power to the demand side is one of the main objectives of microgrids. Therefore, power flow problems such as harmonics and unbalances should be decreased and compensated properly. With a correct approach, controlling power electronics converters can deal with the voltage stability at DC bus in DC microgrids. Then, the controllers

This work is licensed under a Creative Commons Attribution 4.0 License. For more information, see https://creativecommons.org/licenses/by/4.0/

This article has been accepted for publication in a future issue of this journal, but has not been fully edited. Content may change prior to final publication. Citation information: DOI 10.1109/ACCESS.2021.3072899, IEEE Access

can be broadened to DC-AC inverters acting like shunt active filters. Voltage unbalances and harmonic distortion can be weakened at the point of common coupling (PCC) by using hierarchical and distributed controllers. Both grid-connected or standalone mode, microgrids should provide uninterrupted power to the loads, i.e., DC-AC bidirectional converters are employed to provide a stable power to the loads [5]. Some power flow issues are handled against multiple DGs in hybrid AC-DC microgrid by controlling voltage droop in [6]. Besides, synchronization problems should between microgrid and utility grid be addressed undoubtedly. To this end, generally second harmonic based phase locked loop (PLL) is preferred mostly to eliminate this problem [7]. In other words, microgrids can be examined in two groups as a AC and DC type. Compared to the AC microgrids, DC microgrids have apparent advantages such as high efficiency and reliability, low cost, simple control, and flexibility, etc [8]. Besides, frequency synchronization, reactive power control, and skin effect issues do not exist in DC microgrids. Therefore, it is obvious that the applied control schemes of the DC microgrids do not have as more sophisticated as the AC microgrids' one [9]. We also handled design implementation of a DC microgrid. In DC microgrids, an integration of energy storage system can afford a flexible and dynamic energy management system (EMS) to increase the stability and power quality [10], which can be controlled with optimization techniques [11].

On the other hand, since high penetrated renewables are expected to be more feasible in the near future, battery energy storage systems (BESS) will be able to act an important role in terms of reliable and cost-efficient grid-integration of intermittent energy sources. In this context, BESS are indispensable units of DC microgrids. As known, the batteries are operated to mitigate the generated power from the renewables, dispatch smooth power to the loads and increase the level of the scalability [12]. While designing the utilization and lifetime of the BESS should be taken into consideration well due to their total cost of ownership. Some researches show that the batteries should be operated at defined state of charge (*SoC*) level [13]. Also, *SoC* level is recommended lead-acid batteries to operate between 50% and 80% [14]. Hence exhausting and overcharging have bad effects on battery calendar life [15], which should be avoided [16]. For this reason, the *SoC* levels (%) of the batteries should be estimated accurately by some methods such as machine learning [17], model predictive-based power smoothing strategy [18], luenberger observer [19] or kalman filter [20] and they should be run on a band which is protected from over-charge and discharge [21]. To achieve this presumption, it is explicit being necessary to design a charge-discharge controller for confining *SoC* levels and this charge controller should obviously take part in the energy management of the overall system as well.

To eliminate many factors that affect the system operation adversely, notable point is a choice of forming an EMS-based a control algorithm with problem solving methods [22-24]. Accordingly, researches have proposed various EMS approaches such as optimal EMS considering degradation of BESS [25], appointing the optimal scheduling of each DGs [26] to meet power to the demand properly. Using EMS in planning, operation, design, and control of any energy systems needs beginning with a simple flowchart technique, addressing more robust optimization problems, and making the system applicable for different kinds of solutions to new particular situations of interest, is analyzed in detail step by step in [27]. Also in [28], a proposed EMS cooperates to control hybrid power system with the help of power converters. Likewise, another approach-that is, the harmonics are mitigated by controlling currents and voltages of the power converters in a grid integrated hybrid system in [29]. By the way, an effective and convenient control of distribution systems is a critical factor for consumer satisfaction, optimum management of utility grid assets and overall power system performance. Advanced real-time distribution management system applications [30] have been performed such as load distribution, unbalanced load flow, overload prevention, and reactive power-voltage control. Upon investigating all of demanding challenges, lab-scale microgrid test benches [31-33] have become prominent in which contains data acquisition unit for condition monitoring and management through LabVIEW [34] like a human-machine interface.

To meet requirements by providing reasonable approaches to the above-mentioned problems that we face nowadays, the dissemination of renewables and alternative energy sources is one of the most effective remedies. Renewable energy applications based on microgrids are tried to be adapted to the system in different ways both as large-scale systems at the power plant base, laboratory-scale for education purposes or local small-scale systems. These systems emerge as a separate field of investigation and research within the concept of the microgrids, which are vital for power quality, monitoring, and sustainability. Accordingly, complex structures and algorithms including these systems should be flexible in order to use energy resources effectively and properly. To this respect, the main scope of this paper is the studies on some pieces of improvements, modularity, functionality, and problem solving for efficient integration of the flexible structure into the system. To select the optimum EMS algorithm for smooth power flow, one should first understand the core of the power flow and the type of design structure that is being discussed. This study aims to model and establish a laboratory-scale microgrid system that can tackle possible power challenges in simple ways. Also, we elucidate to produce effective power with fewer losses in order for meeting the energy efficiency from DGs to the loads. The aforementioned system, an education, and research laboratory at which the experimental setup has been installed our University, is situated for the students and researchers.

The rest of this paper is organized as follows: the description and modeling of the whole proposed microgrid

This work is licensed under a Creative Commons Attribution 4.0 License. For more information, see https://creativecommons.org/licenses/by/4.0/

This article has been accepted for publication in a future issue of this journal, but has not been fully edited. Content may change prior to final publication. Citation information: DOI 10.1109/ACCESS.2021.3072899, IEEE Access

system is handled in Section II. The control scheme of this system is depicted in Section III. Energy management algorithm and a case study belong to the system are designed in Section IV. The results of simulation and experimental setup are also presented in Section V and VI, respectively, and finally the paper is concluded in Section VII.

II. DESCRIPTION AND MODELING OF LAB-SCALE MICROGRID

As can be seen in Fig. 1, the system contains a photovoltaic (PV) array, a wind turbine, a fuel cell unit, and a battery bank as RESs, power electronic converters, filters, and loads. Fig. 1 depicts the laboratory-scale microgrid system is discussed. The rated power of PV array is equal to 1 kW and is designed by a single diode model. A maximum power point tracking (MPPT) control extract maximum power from the solar panel using a unidirectional DC-DC boost converter. To keep up with a maximum power point (MPP) calculated by the MPPT algorithm, a cascade control mechanism drives a DC-DC converter. The cascade control mechanism is a series of voltage and pulse width modulation (PWM) controller.

While the PV array and wind turbine are the main power source, the battery bank is specified as a complementary power source. The fuel cell unit is for educational purposes and is activated through an electrolyser that is operated with surplus energy after the load shedding. In other words, if the *SoC* has an optimum value, the electrolyser is operated and then the metal hydride H_2 tube is filled for supplying the fuel cell unit. Thereby, the fuel cell unit is supplied with H_2 gas which is produced by the electrolyser and also has a compact DC-DC converter and DC load. The PV array is connected to the DC bus through a unidirectional DC-DC boost converter, while the battery bank is connected to the same bus with a bidirectional DC-DC buck boost converter. Besides, the wind energy conversion system is also connected to the system in the same way as the PV array. With regards to the main power source, the BESS contains six pieces of batteries, three pieces connected in parallel and two pieces of them in series. Meanwhile, the utility grid is another main power supply. The utility grid feeds the loads while the produced power is insufficient and the *SoC* level of the battery bank is lower than the defined healthy value, which means operating in grid mode. The connection between the utility grid and the microgrid is controlled by a bidirectional interlinking DC-AC inverter. As can be shown in Fig. 1, the utility grid is connected to the laboratory from a pole-mounted distribution transformer. Protective diodes have been settled to prevent the connected DGs within the model from being exposed to a negative reverse current from the DC bus. In other respect, the parameters of the system components belong to laboratory-scale microgrid system are given in Table 1.

Basically, it can be considered that that laboratory-scale microgrid realizes the power flow through power electronics converters with the help of an EMS based on system controllers. In the proposed system, the mathematical models of each component are imperative for designing a sophisticated EMS to be able to embed the control algorithms. While modeling the electrical behavior of the system, their structure should be well known before being operated in a variety of applications. Thereby, we modeled the system to test under many scenarios and validate the control methodology. Certainly, the models are a facilitated and limited (i.e., only electrical) representation of our real systems.

A. SOLAR ENERGY CONVERSION SYSTEM

As mentioned, the solar energy conversion system comprises a PV array and a boost converter which is operated by the MPPT-based controller. Before proceeding, the components of the PV system are important to mention. Upon explaining PV generation, all units and factors which affect the amount of generation should be taken into properly. Essentially, the PV generation is affected through solar irradiance and temperature as inputs.

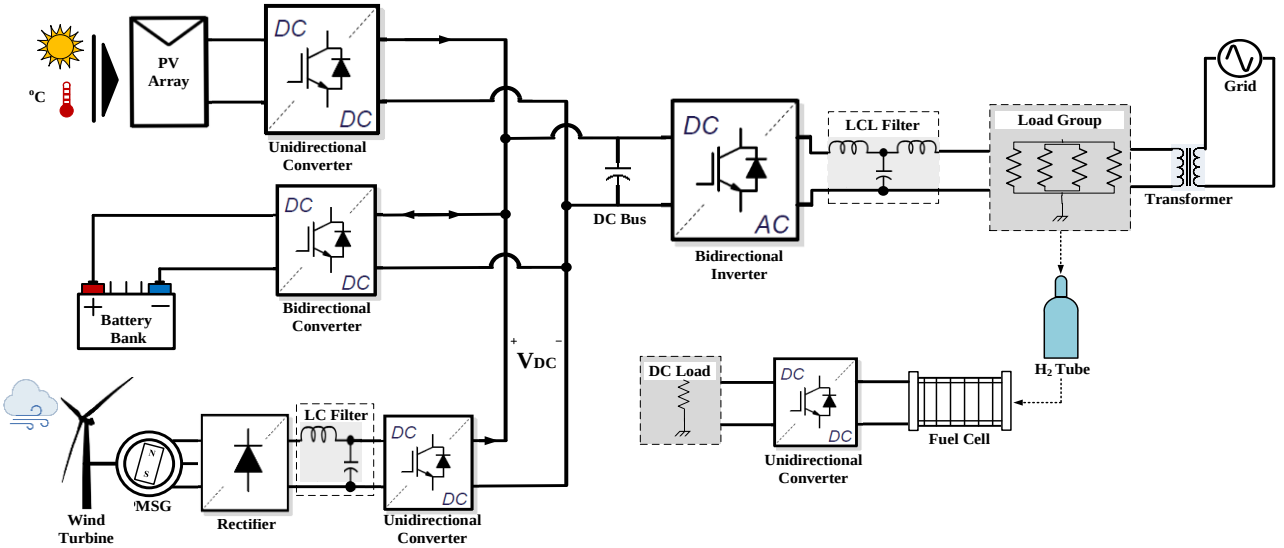

FIGURE 1. Description of proposed education laboratory-scale microgrid.

This work is licensed under a Creative Commons Attribution 4.0 License. For more information, see https://creativecommons.org/licenses/by/4.0/

This article has been accepted for publication in a future issue of this journal, but has not been fully edited. Content may change prior to final publication. Citation information: DOI 10.1109/ACCESS.2021.3072899, IEEE Access

As known, a PV panel comprises of combining PV cells which are simply a *p-n* junction semiconductor. Additionally, PV arrays are known to be formed with PV panels. Due to having variable inputs such as solar irradiance and temperature, accurate modeling of these nonlinear structure is vital. So, we have selected a five parameter (single diode) model for the model of PV as an equivalent circuit of a PV cell, as shown in Fig. 2. As long as the output current of the cell (I_{CELL}) can be calculated with (2) according to the Kirchhoff's laws.

$$-I_{CELL} - I_{SH} + I_{PH} - I_D = 0 \tag{1}$$

and

$$I_{CELL} = I_{PH} - I_0\left(e^{\frac{V_{CELL}+I_{CELL}R_S}{nVt}} - 1\right) - \frac{V_{CELL}+I_{CELL}R_S}{R_{SH}} \tag{2}$$

$$V_t = \frac{nkT_{STC}}{q} \tag{3}$$

TABLE 1. Components of energy conversion systems.

PV Array	
Rated Maximum Power-*Pm* (kW)	1
Maximum Power Current-*Imp* (A)	32.68
Maximum Power Voltage-*Vmp* (V)	30.6
Short Circuit Current-*Isc* (A)	34.83
Open Circuit Voltage-*Voc* (V)	36.3
Module Efficiency-η (%)	15.40
Wind Turbine	
Turbine Type	Horizontal Axis
Rotor Diameter (m)	1.17
Blades	(3) Injection moulded comp.
Generator Type	Permanent magnet sync.
Start-up Wind Speed (m/s)	3.58
Survival Wind Speed (m/s)	49.2
Output Voltage (V)	24
Rated Power (W)	400
Battery Bank	
Battery Type	Lead-Acid
Nominal Voltage (V)	12
Nominal Capacity (Ah)	200
Internal Resistance (mΩ)	3.4
Cut-off Voltage (V)	9
Fully Charge Voltage (V)	13.9
Fuel Cell	
Nominal Power (kW)	1.2
Rated Current (A)	65
Operating Voltage (V_{DC})	20-35
Number of Cells	36
Efficiency	46
Max H_2 consumption (sl/min)	15

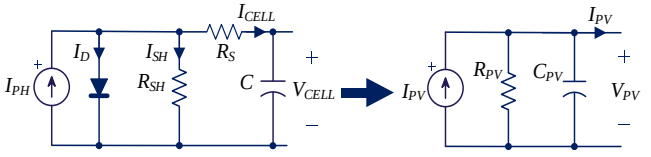

FIGURE 2. Equivalent circuit of a PV panel (single diode model).

The five unknown parameters are as follows: the photo generated current at (standard test conditions) STC-I_{PH}, diode saturation current at STC-I_0, series resistance-R_S, shunt resistance-R_{SH}, and diode ideality factor-*n* that have not found in the datasheets; however, can be extracted from datasheet values indirectly [35] or can be estimated with one of some methods like Bisection and Lambert-W existing in [36, 37].

For the other parameters of the model, expressed in (3), V_t defines the cell equivalent thermal voltage, *q* denotes the electron charge, *k* identifies to boltzmann constant, and T_{STC} (^{o}K) belongs to reference temperature at STC. As referred before, the PV array includes one series module and four parallel strings along with each panel has 250 W. Thereby, the total rating power corresponds to 1 kW. As indicated, the solar energy conversion system has been aimed to design with a unidirectional DC-DC boost converter which is controlled by the MPPT algorithm to more harvest the natural power comes from the sun against variable inputs. Thus, extracting the maximum power from PV array have been targeted. Essentially, a MPPT algorithm is operated in the converter control adjusting reference PV voltage i.e., V_{REF} to maximize the energy yield as much as possible in any case. Besides, the MPPT algorithm is operated with a proportional-integral (PI) control that produces a duty cycle to get started PWM by sensing the difference between a reference produced voltage-V_{PV} and current-I_{PV}. So, the maximum power from PV arrays to DC bus is supplied efficiently.

One of the most preferred MPPT algorithm is perturb and observe (P&O) has been preferred. That method determines the change in power at the voltage-power characteristic of the PV structure. If the change of power, i.e., *dP/dV* is positive, it can be deduced that the current power is on the left side of the MPP, otherwise, *dP/dV* is negative, current power is on the right side of the MPP.

$$\left.\frac{dP}{dV}\right|_{P=P_{MPP}} = 0 \tag{4}$$

Thus, it is expected to reach the MPP (i.e., the hill) by being determined in which direction the current power should be approached. These methods are simple and convenient to apply to the PV systems [38].

B. WIND ENERGY CONVERSION SYSTEM

This system includes a wind turbine, a permanent magnet synchronous machine (PMSM) as a generator, a diode rectifier with an LC filter, and lastly a unidirectional DC-DC converter. The wind turbine also dispatches its power to the DC bus with these components. The output of this DC power has a voltage-current regulator with a PI controller. Three phase PMSG is embedded into the wind turbines. The wind speed profile does not have too much fluctuation in the given place. The turbine has small rated power; nevertheless, to harvest wind turbine power at the desired level, a boost converter has been preferred.

Essentially, the wind energy conversion system has been designed as five parts. The wind turbine of this system consists of a horizontal axis turbine of three blades with zero pitch angle (β). It is highly not recommended to connect a synchronous generator directly to the network

This work is licensed under a Creative Commons Attribution 4.0 License. For more information, see https://creativecommons.org/licenses/by/4.0/

This article has been accepted for publication in a future issue of this journal, but has not been fully edited. Content may change prior to final publication. Citation information: DOI 10.1109/ACCESS.2021.3072899, IEEE Access

unless it has a variable gear system. For this reason, synchronous generators preferred in wind power applications in the market are connected to the system with a full-scale power converter [39]. Although this full-scale power converter can provide smooth power flow at variable wind speeds, it is undeniable that the cost and power loss will be able to increase. The synchronous generators are extensively used for variable wind speed in wind turbine applications owing to their low rotation synchronous speeds that can comply with the grid frequency. It is sensible to be preferred in these applications, once the wind speed possesses much more variance [40, 41].

The maximum value of phase voltage is V_m, average output of the rectifier voltage V_o is V_{DC} and it can be defined as

$$V_{DC} = \frac{1}{T}\int_0^T V_0(t)dt \tag{5}$$

Exploiting (5), the average voltage of the output $V_{DC\text{-}out}$ can be found as

$$V_{DC-out} = \frac{6}{2\pi}\int_{\pi/3}^{2\pi/3} \sqrt{3}V_m \sin\theta d\theta \tag{6}$$

or

$$V_{DC-out} = V_m \frac{3\sqrt{3}}{\pi} = 1.654V_m \tag{7}$$

An LC filter has been used to suppress high frequency harmonics coming from the diode rectifier. We can see that it is filtered through an LC filter to eliminate harmonics and obtain purer DC without oscillations for transferring smooth power to the DC bus. The cut-off frequency (f) of the LC filter can be given by

$$f = \frac{1}{2\pi\sqrt{LC}} \tag{8}$$

The wind turbine power characteristics versus wind speed are shown in Fig. 3. The turbine output power can be counted as being 320 W for 0.8 per unit of nominal mechanical power, so the nominal rated output power denotes 400 W at base wind speed. The stiffness of the drive train is infinite and the friction factor and the inertia of the turbine should be combined with those of the generator coupled to the turbine. The output power of the turbine is given as

$$P_m = C_p(\lambda,\beta)\frac{\rho A}{2}v_{wind}^3 \tag{9}$$

where, C_p is the function of the turbine's performance coefficient, ρ is air density (kg/m^3), A is the turbine swept area (m^2), V_{wind} the wind speed (m/s), λ is tip speed ratio of the rotor blade tip speed to wind speed, β the blade pitch angle (degree) and P_m is Mechanical output power of the turbine (W). Equation (10) is utilized to model C_p (λ, β) that based on the modeling turbine specifications [42].

$$C_p(\lambda,\beta) = c_1(c_2/\lambda_i - c_3\beta - c_4)e^{-c_5/\lambda_i} + c_6\lambda \tag{10}$$

with

$$\frac{1}{\lambda} = \frac{1}{\lambda + 0.08\beta} - \frac{0.035}{\beta^3 + 1} \tag{11}$$

As known, the coefficients and the turbine characteristics can vary for different values of the pitch angle β. The model of the permanent magnet synchronous generator (PMSG) is based on (12) in d-q frame. Besides, the electromagnetic torque of the generator T_{em} can be formulated as (11) provided that L_q is equal to L_d,

$$\begin{bmatrix} V_d \\ V_q \end{bmatrix} = \begin{bmatrix} R_c & -\omega L_c \\ \omega L_c & R_c \end{bmatrix} * \begin{bmatrix} i_d \\ i_q \end{bmatrix} + L_c \frac{d}{dt}\begin{bmatrix} i_d \\ i_q \end{bmatrix} + \begin{bmatrix} e_d \\ e_q \end{bmatrix} \tag{12}$$

$$T_{em} = P\varphi i_q \tag{13}$$

Regarding to the model of the PMSG by (12), the Clarke transformation is taken into consideration, so the PMSG model in α-β frame can be expressed as

$$\begin{bmatrix} \dot{i}_\alpha \\ \dot{i}_\beta \end{bmatrix} = \begin{bmatrix} \frac{-R_s}{L_s} & 0 \\ 0 & \frac{-R_s}{L_s} \end{bmatrix} * \begin{bmatrix} i_\alpha \\ i_\beta \end{bmatrix} + \begin{bmatrix} \frac{1}{L_s} & 0 \\ 0 & \frac{1}{L_s} \end{bmatrix} \begin{bmatrix} V_\alpha - e_\alpha \\ V_\beta - e_\beta \end{bmatrix} \tag{14}$$

$$e_\alpha = -\omega\varphi\sin\theta \tag{15}$$

$$e_\beta = \omega\varphi\cos\theta \tag{16}$$

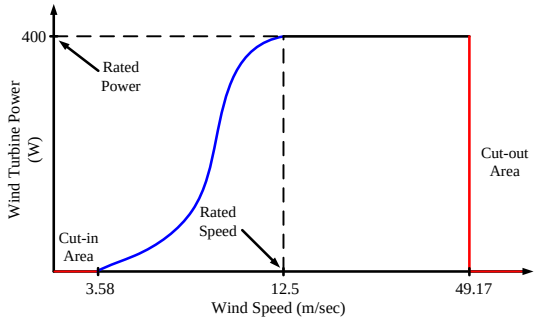

FIGURE 3. Turbine power characteristic versus wind speed.

where, V_d-V_q and V_α-V_β are stator voltage vectors, i_d, i_q and i_α-i_β are stator current vectors, e_d-e_q and e_α-e_β are direct and quadratic magnetic electromotive forces, respectively. R_c is resistance of each stator phase. ω is the rotor electrical angular speed, φ is the permanent magnetic flux, and lastly L_c is inductance of each stator phase.

C. ENERGY STORAGE UNIT (BATTERY BANK)

In autonomous microgrids, batteries are broadly preferred for supplying power as an energy storage device [23]. Similarly, for islanded or grid-connected operation, the need for an optimal energy storage unit is indispensable in order to stabilize the power, mitigate the output of the DG systems like solar and wind, supply the power to the loads when DGs are deprive of generation and provide a smooth power to the demand side [43].

Due to its long lifetime and costs per capacity, Lead Acid is among the electrochemical energy storage devices highly preferred in the industry. Since the Lead Acids has high volume and weight per usable kWh compared to the other battery types, they are broadly preferred for the static applications unlike electric vehicles [44]. However, the used battery does not discharge wholly, rather, they have a

This work is licensed under a Creative Commons Attribution 4.0 License. For more information, see https://creativecommons.org/licenses/by/4.0/

This article has been accepted for publication in a future issue of this journal, but has not been fully edited. Content may change prior to final publication. Citation information: DOI 10.1109/ACCESS.2021.3072899, IEEE Access

recommended depth of discharge (DoD) which means how much can be used before it should be recharged. Lead-acid batteries should be consumed to nearly 50% DoD. Beyond this value, their lifetime is affected negatively.

The batteries can be classified into different three kinds of model such as electrochemical, mathematical, and equivalent electric circuit model. The mathematical generic model has been used in this paper for fast battery model development based on datasheet values, which is also equal to the model in [45]. Fig. 4 illustrates the equivalent circuit model of the battery. This model belongs to a variable battery voltage (V_{Batt}) that can be expressed in both two modes such as discharge and charge for lead acid battery, with the help of a bidirectional DC-DC buck-boost converter.

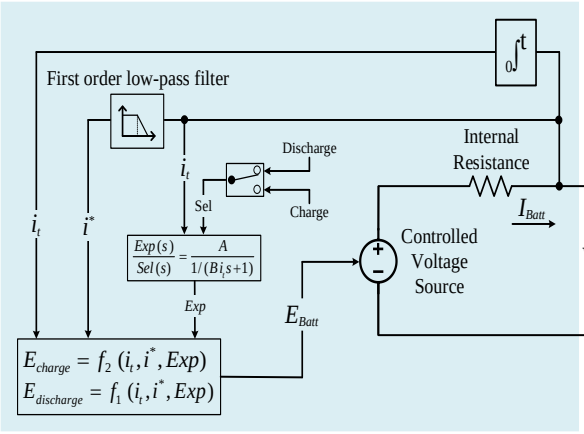

FIGURE 4. **Equivalent mathematical generic circuit model of the battery.**

The parameters can be adjusted to exemplify a battery type and its discharge characteristics. A typical discharge curve is formed of three parts. The first part illustrates the exponential voltage drop once the battery is charged. The shape of the drop changes with the battery type. The second part examples the charge that can be obtained from the battery until the voltage drops below the battery nominal voltage. Finally, the third one exemplifies the total discharge of the battery, when the voltage drops swiftly. While (17) denotes the function of discharge for the battery, (18) expresses the function of charge.

$$V_{Batt} = E_0 - R_{Batt} i_{Batt} - K\frac{Q}{Q - i_{Batt}t} i_{Batt}t - K\frac{Q}{Q - i_{Batt}t} i^* + \exp(t) \quad (17)$$

$$V_{Batt} = E_0 - R_{Batt} i_{Batt} - K\frac{Q}{Q - i_{Batt}t} i_{Batt}t - K\frac{Q}{i_{Batt}t - 0.1Q} i^* + \exp(t) \quad (18)$$

where, A is exponential zone voltage (V), B is exponential zone inverse capacity ((Ah)$^{-1}$), E_0 is battery constant voltage (V), R_{Batt} is internal resistance (Ω), i_{Batt}t actual battery charge (Ah), i_{Batt} (A) is battery discharge current, K is polarization constant (V/(Ah)), i^* is low-frequency current dynamic (A), Q is nominal or rated battery capacity (Ah). The *SoC* values of the batteries can be calculated with ampere-hour (coulomb) counting method. In this method, it is assumed that the battery capacity is known and battery parameters like voltage and current can be measured accurately. On the other hand, a full cycle is defined as complete discharge and charges to 100% *DoD* is expressed as

$$SoC = 1 - DoD \quad (19)$$

As known, if the *SoC* has 100% value or is equal to 1, it represents a fully charged battery and 0% means an empty battery. SoC_i is initial value of the *SoC* which is formulated as

$$SoC = SoC_i - \frac{1}{Q}\int_{t_2}^{t_1} i_{Batt}\,dt \quad (20)$$

It is worth mentioning that the battery bank has been established on behalf of the energy storage unit that includes 6 pieces of battery. One single battery has 200 Ah capacity and its output voltage is 12 V. Consequently, as 3 pieces of parallel and 2 pieces of series connection enable the battery bank that it corresponds 600 Ah capacity, 24 V with an output voltage and also 14.4 kWh with an energy capacity.

D. FUEL CELL CONVERSION SYSTEM

In these systems, without the utilization of a boiler or turbine, the electrical energy is generated by the flow of electrons only as a result of chemical reactions from the fuel cells [46]. The total efficiency obtained by the electrochemical reaction between hydrogen (H_2) and oxygen (O_2) can reach up to 80%. Therefore, the exploitation of the fuel cells is primarily due to their high-reliability performance, cheap maintenance price, and low emission of pollutants [47]. We have used the detailed preferred a generic model of the fuel cell stack that has an internal resistance and diode, are fed by hydrogen and air. This model corresponds to the fuel cell equivalent model shown in Fig. 5. The fuel cell conversion system is also connected to the DC bus via a unidirectional DC-DC boost converter which is controlled by a PI voltage reference controller since it does not generate fully stable output characteristics like the other DG systems.

$$E = E_{oc} - NA\ln\left(\frac{i_{fc}}{i_0}\right)\frac{1}{sT_d/3+1} \quad (21)$$

$$V_{fc} = E - R_{\text{int}} i_{fc} \quad (22)$$

where, E_{OC} is an open circuit voltage (V), N is number of cells, A is Tafel slope (V) related activation kinetics of the fuel cell, i_0 is an exchange current (A), T_d is a response time (sec), R_{int} is an internal resistance (Ω) of the fuel cell model, finally i_{fc} and V_{fc} is generated fuel cell current (A) and voltage (V), respectively.

Equation (21) exists in [48], is also related to (23) and (25) that represent activation losses the stack voltage. These losses have been modeling electrically with a parallel RC branch. Unforeseen variation in stack current, the fuel cell voltage displays a time delay ($\tau = RC$) that is nearly three times the time constant prior to steady-state. Because of this phenomenon, it includes with a first order transfer function $1/(sT_{d/3}+1)$.

This work is licensed under a Creative Commons Attribution 4.0 License. For more information, see https://creativecommons.org/licenses/by/4.0/

This article has been accepted for publication in a future issue of this journal, but has not been fully edited. Content may change prior to final publication. Citation information: DOI 10.1109/ACCESS.2021.3072899, IEEE Access

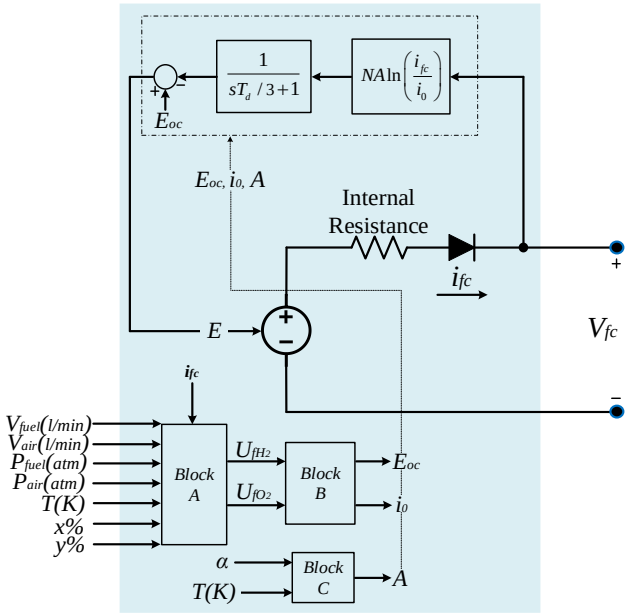

FIGURE 5. **Detailed fuel cell model.**

Also, (22) gives the total stack voltage resulting from the ohmic losses. This detailed model represents the fuel cell stack which exhibits a certain behavior in response to changes in temperature, pressure, fuel and airflow rate, hydrogen content in the fuel, and oxygen content in the oxidant. These changes are the open-circuit voltage (E_{OC}) of the stack, the exchange current (i_0), and the tafel slope (A) [49].

$$E_{oc} = K_c E_n \tag{23}$$

$$E_n = 1.229 + (T - 298)\frac{-44.43}{zF} + \frac{RT}{zF}\ln\left(\frac{P_{H_2} P^{0.5}}{P_{H_2O}}\right) \tag{24}$$

$$i_0 = \frac{zFk(P_{H_2} + P_{O_2})}{Rh}\exp\left(\frac{-\Delta G}{RT}\right) \tag{25}$$

$$A = \frac{RT}{z\alpha F} \tag{26}$$

where, E_n is Nernst voltage (V), K_c is voltage constant at nominal condition of operation, P_{H2} and P_{O2} are partial pressure of hydrogen and partial pressure of oxygen inside the stack (atm), respectively. As to constants, k is Boltzmann's constant (1.38×10^{-23} J/K), h is also Planck's constant (6.626×10^{-34} J s), R is equal to 8.3145 J/(mol K), F is 96485 A s/mol. ΔG is activation energy barrier (J), T is temperature of operation (K), and finally α is charge transfer coefficient, z is number of moving electrons. As can be seen in Fig. 5, according to inputs, the new values of E_{OC}, i_0, and A are derived from using block A, B, and C. In block A, the rates of the use of hydrogen (U_{fH2}) and oxygen (U_{fO2}) can be expressed as

$$U_{fH_2} = \frac{60000RTi_{fc}}{zFP_{fuel}V_{fuel}x} \tag{27}$$

$$U_{fO_2} = \frac{60000RTi_{fc}}{2zFP_{air}V_{air}y} \tag{28}$$

where, P_{fuel} and P_{air} are pressure of fuel and absolute pressure of air (atm), V_{fuel} and V_{air} fuel flow rate and air flow rate (l/min) x and y are percentage of hydrogen (%) in the fuel and oxygen (%) in the oxidant, respectively. By all means, it is required to inspect this fuel rate (l/min) of the fuel cell from the hydrogen tank, so a fuel rate regulator has been designed based on (23) with the feedback of the current for nominal flow rate (V_{lpm}).

$$V_{lpm} = \frac{60000RTNi_{fc}}{2zFP_{air}U_{fH_2}x} \tag{29}$$

Thereby, the fuel cell stack generates a DC voltage. As can be seen from Fig. 6, the typical polarization (voltage-current) curve consists of three zones. The first zone indicates the reduction of the activation voltage due to the duration of the chemical reactions that occur on the electrode surface. The second zone describes the resistive loss due to internal resistance in the stack, while the third zone describes mass transport losses due to changes in the concentration of reactants with resulting in fuel utilization [50].

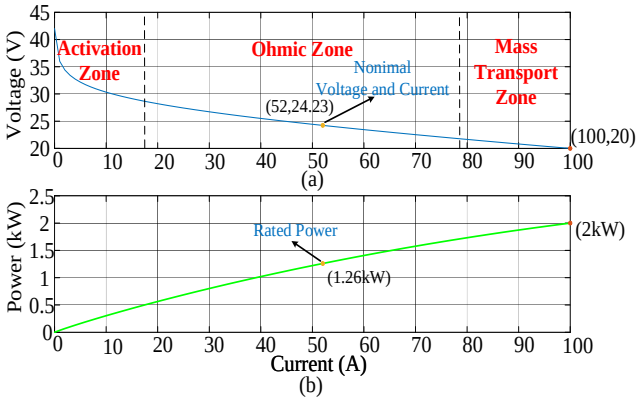

FIGURE 6. **(a) V-I and (b) P-I characteristic curves of fuel cell stack used in the model.**

E. INTERLINKING BIDIRECTIONAL DC-AC CONVERTER AND LOAD GROUPS

The bidirectional DC-AC converter is the fundamental converter of the system. In addition to being the unit that transfers the power generated from the DGs and thus from the DC bus to the loads, the smooth transfer of the power is performed in this unit. On the load side of the system towards the grid side, the existing LCL filter which diminishes the high-frequency current harmonics. While designing, if the PWM's carrier frequency is set, then the cut-off frequency of LCL is designed to be smaller than the carrier frequency to practice enough attenuation for the harmonics near the carrier frequency and further reduce the current ripple. The mathematical model of the designed bidirectional DC-AC inverter can be described neglecting the filter capacitor (C),

This work is licensed under a Creative Commons Attribution 4.0 License. For more information, see https://creativecommons.org/licenses/by/4.0/

This article has been accepted for publication in a future issue of this journal, but has not been fully edited. Content may change prior to final publication. Citation information: DOI 10.1109/ACCESS.2021.3072899, IEEE Access

$$V_L = V_G + R_T I_L + L_T \frac{dI_L}{dt} \tag{30}$$

$$I_L = I_f + I_C = I_f + C\frac{dV_L}{dt} \tag{31}$$

where, L_T=L_f+L_G, R_T=R_f+R_G, V_L is the grid voltage, I_L is the grid current, and I_f is the converter side current. The LCL filter is made up of with inductance L_f and resistance R_f on the converter side, another inductance L_G and resistance R_G on the grid side, and finally capacitor (C_f) damped by RC.

The neat design of the LCL filters is an important consideration for achieving high quality grid current. The LCL parameters can be calculated from the following equations so that the converter and the grid can operate together in desired harmony [51]. Also, the unipolar PWM approach has triggered the switches to perform the inverter.

$$Z_B = \frac{(E_n)^2}{P} \tag{32}$$

for capacitor,

$$C_B = \frac{1}{\omega_G Z_B}$$

with

$$C_f \le 0.05 C_B \tag{33}$$

where, the capacitor value of the filter (C_f) is restricted by the reduction of the power factor (less than 5%) in the rated capacity. k_a is an attenuation factor, should be taken as 0.2 [52].

$$I_{\max} = \frac{\sqrt{2}P}{3V_f} \tag{34}$$

$$\Delta I_{L\max} = 0.1 I_L \tag{35}$$

The average rated current is presumed to fluctuate by 10% in (33). Where Z_B is base impedance, E_n is one phase effective voltage, P is active power, C_B is base capacitance, ω_G is grid angular velocity, V_f is filter voltage, f_{SW} is switching frequency. So, the values of the inductors can be expressed as

$$L_f = \frac{V_{DC_Bus}}{6 f_{SW} \Delta I_{L\max}} \tag{36}$$

$$L_G = \frac{1 + k_a}{k_a C_f \omega_{SW}^2} \tag{37}$$

The parameters of the designed inverter are presented in Table 2. Furthermore, the DC bus capacitor are calculated as follows

$$C_{DC_Bus} = \frac{I_{DC}}{2\omega \Delta V_{DC_Bus}} \tag{38}$$

The average daily energy consumption of the load groups and appliances of the system are expressed in Table 3. Totally, four kinds of loads of 1670 W include power supply of 600 W, lighting armature of 520 W, electrolyser of 300 W, multimeter of 250 W, which can be connected to the microgrid. They consume a total of 1670 W of electrical power when all are connected.

TABLE 2. Parameters of the bidirectional interlinking inverter.

Element	Value
DC bus voltage	370 V
Grid voltage (RMS)	230 V
Grid frequency	ω =2 π 50 rad/s (50 Hz)
Switching frequency	10 kHz
DC bus capacitor	118.28 μF
LCL filter	L_f=1.2034 mH, L_G=*9.244* μH, C_f=*8.22* μF

TABLE 3. Load Profile.

Appliance	Peak Power (W)	Operation Times (s)
Lighting Armatures	520	0.05 s - 0.15 s & 0.25 s - 0.35 s
Power Supply	600	0.10 s - 0.15 s & 0.30 s - 0.35 s
Electrolyser	300	0.45 s - 0.62 s
Multimeter	250	0.50 s – 0.70 s

III. SYSTEM CONTROL SCHEME

Proper control of power converters does not solely have traditional multiple feedback loops, besides PWM is essential. The controller is one of system's the main parts for achieving a high-performance. The general configuration and control structure of the solar energy conversion system with a unidirectional DC-DC boost converter which depicts acquiring the maximum power from the PV array. The MPPT algorithm, which detects the generated array current and voltage, generates a reference voltage. This reference voltage is controlled by the PI controller according to the instantaneous voltage value, which enables the PWM signal to be sent to the converter. To obtain maximum accuracy with dynamism, the step size has been selected as 0.01 V for P&O MPPT algorithm. The switching frequency is realized for PV converter, is 10 kHz.

Before progressing, it is notable to explain about acquiring the necessary transfer functions for controllers after making simpler and linearizing the modeled system. R_{PV} is equal to V_{PV}/I_{PV}, which is output resistance of the PV array, the transfer function between the converter input voltage (V_{PV}) and the duty cycle (D) is stated through the small-signal model as

$$\frac{V_{PV}(s)}{D(s)} = \frac{\frac{-V_{DC}}{LC_{PV}}}{s^2 + \frac{s}{R_{PV}C_{PV}} + \frac{1}{LC_{PV}}} \tag{39}$$

Let us now consider about the rectifiers are widely categorized as controlled and uncontrolled with regards to rectifiers. The uncontrolled full-bridge rectifier utilizes only diodes as switching semiconductor devices in applications, where the control of power flow is not compulsory. Nevertheless, thyristors, MOSFETs or IGBTs can be preferred in a controlled rectifier to manage the power flow. Therefore, the uncontrolled full-bridge rectifier structure has been used with an LC filter to obtain power from the

This work is licensed under a Creative Commons Attribution 4.0 License. For more information, see https://creativecommons.org/licenses/by/4.0/

This article has been accepted for publication in a future issue of this journal, but has not been fully edited. Content may change prior to final publication. Citation information: DOI 10.1109/ACCESS.2021.3072899, IEEE Access

turbine due to the low peak power of the wind conversion system. With the aim of obtaining smooth power through an LC filter, the ongoing power to the DC bus is controlled by a unidirectional DC-DC boost converter. Similarly, the output resistance of the WT i.e., R_{WT} is equal to V_{WT}/I_{WT}, the transfer function between the converter input voltage (V_{WT}) and D is stated by the small-signal model as follows

$$\frac{V_{WT}(s)}{D(s)} = \frac{\frac{-V_{DC}}{LC_{WT}}}{s^2 + \frac{s}{R_{WT}C_{WT}} + \frac{1}{LC_{WT}}} \tag{40}$$

In this study, the energy storage unit comprises of lead-acid batteries and bidirectional DC-DC buck-boost converter that is tied to the DC bus to provide the power to the loads permanently, once nonproducing inputs occurs. The utilization of this bidirectional DC-DC buck-boost converter aims keeping the DC bus voltage, while the voltage changes based on production and consumption. This utilization is gone through controlling both the DC bus voltage and the battery current with cascaded-PI controller. That cascaded structure is divided two parts regarding DC bus voltage and current controller. The switching frequency has been achieved for this converter as10 kHz. The modes of the bidirectional DC-DC buck-boost converter which performs two different modes such as buck and boost mode. Whereas the buck mode corresponds charging, the boost mode does discharging of the battery bank. Assuming that the dc bus voltage denotes $V_{DC,}$ so $R_{DC}=P_{DC}/(I_{Bat})^2$ is the output resistance of the battery bank, and the transfer function between the converter input voltage (V_P) and D can be defined as

$$\frac{V_{DC}(s)}{I_{BAT}(s)} = \frac{(1-D)(R_{DC}-sL)}{1+(sR_{DC}C_{DC})+(1-D)^2} \tag{41}$$

$$\frac{I_{BAT}(s)}{D(s)} = \frac{2R_{DC}+sR_{DC}{}^2C_{DC}}{s^2LC_{DC}R_{DC}+sL+R_{DC}-2DR_{DC}+R_{DC}D^2} * \frac{V_{BAT}}{R_{DC}(1-D)} \tag{42}$$

The control of the fuel cell unit is achieved through a unidirectional DC-DC boost converter, existing with a PI reference voltage controller and also a flow rate regulator which adjusts the fuel flow. Where, $R_{FC}=V_{FC}/I_{FC}$ is output resistance of the fuel cell, the transfer function between the converter input voltage (V_{FC}) and D can be expressed as follows

$$\frac{V_{FC}(s)}{D(s)} = \frac{\frac{-V_{DC}}{LC_{FC}}}{s^2 + \frac{s}{R_{FC}C_{FC}} + \frac{1}{LC_{FC}}} \tag{43}$$

On the grid side, bidirectional DC-AC inverter dispatches obtained the power to load groups adjusting the DC bus voltage and providing the grid synchronization through PLL, in addition, controlling the grid current as well. As known, PLL is a nonlinear feedback control system that synchronizes its output in frequency and phase with its input [53]. The designed values of PI controllers' gains are given in Table 4.

TABLE 4. Parameters of the PI controller gains.

Conversion System	Value
PV Array	
Outer Loop	Kp= 0.0500, Ki=10
Inner Loop	Kp= 0.025, Ki=10
Battery Bank	
Outer Loop	Kp= 0.400, Ki=2
Inner Loop	Kp= 0.1, Ki=0.5
Fuel Cell	
Boost voltage control	Kp= 0.0050, Ki=0.15
Inverter	
Outer Loop	Kp= 0.010, Ki=25
Inner Loop	Kp= 0.1, Ki=0.5
Synchronization (PLL)	Kp= 180, Ki=3200, Kd=1

Fig. 7 shows the general control structure of the whole system. It is visible that energy management requirements affect the switches belong to bidirectional DC-DC buck-boost converter and bidirectional DC-AC inverter, in terms of charging or discharging related to the system modes. The system control with the EMS requirements has been performing based on the system mode such as battery or grid mode with the aid of some pieces of the circuit breakers and relays. Briefly, cascaded-PI reference voltage-current controller structure has not been only preferred to obtain good results, but also this controller structure is selected as one of the most common controllers in the industry to implement this conformation to the mentioned system.

IV. ENERGY MANAGEMENT SYSTEM

As previously stated, the EMS has two different modes. In battery mode, the batteries are fed by DGs and thereafter the loads are also. Despite the batteries discharge up to a certain SoC_{min} level, the inverter dispatches the power to the loads in battery mode. Moreover, in this mode, the grid is untied. On the contrary, in grid mode, if the *SoC* level is lower than minimum value i.e., SoC_{min}, the batteries need to be charged and then is charged by the grid. The flow chart of the EMS can be stated in Fig. 8. If *SoC* value reach more than SoC_{max}, the electrolyser is performed and also the loads can be fed if needed.

Primarily, it is better to mention about charger and output sources priorities. The EMS enables prosumer to define priorities for the system operation. The output source priority can be examined with three matters as 1) *solar*, 2) *SBU* (i.e., solar-battery-utility grid), and lastly 3) *utility grid*. Similarly, the charger source priority is divided into three matters such as I) *utility grid*, II) *solar-first*, and III) *utility grid* & *solar* selections. After this selection, it is required to define the initial *SoC* boundaries as SoC_{min} and SoC_{max}.

While the charge source selection provides the batteries to be charged to related selection, the output source selection prioritizes the generation point that dispatches the power to the loads through the inverter.

This work is licensed under a Creative Commons Attribution 4.0 License. For more information, see https://creativecommons.org/licenses/by/4.0/

This article has been accepted for publication in a future issue of this journal, but has not been fully edited. Content may change prior to final publication. Citation information: DOI 10.1109/ACCESS.2021.3072899, IEEE Access

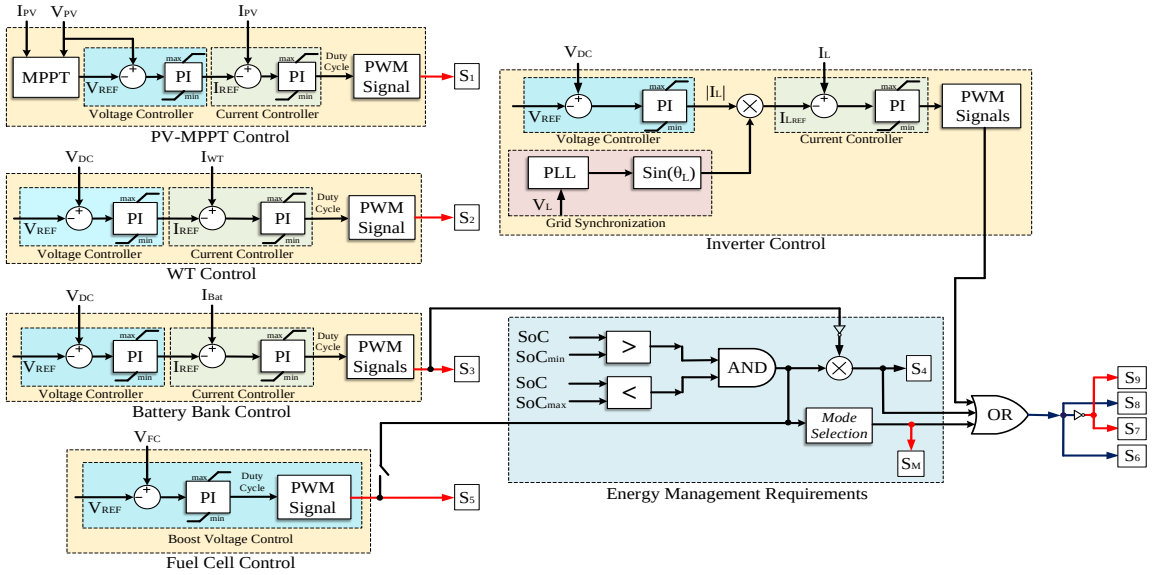

FIGURE 7. **Proposed control structure.**

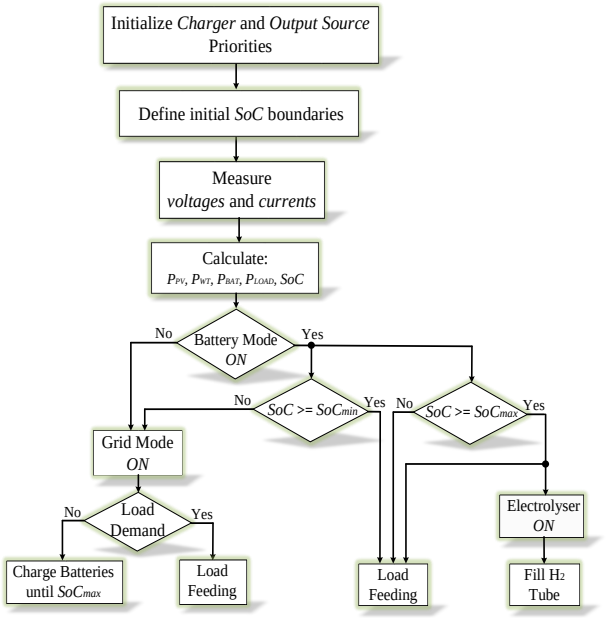

FIGURE 8. **Flow chart of energy management system.**

Since the mentioned system has a big potential power of solar PV, solar power is prioritized to feed the loads permanently. The power in the system under variable input and output i.e., load conditions can be equilibrated as

$$P_{NET} = \begin{cases} P_{BAT}, & \text{if } \mathrm{SoC}_{min} \le SoC \le \mathrm{SoC}_{max} \ \text{(Battery Mode ON)} \\ P_{LOAD}, & \text{if } SoC \le \mathrm{SoC}_{min} \ \text{(Grid Mode ON)} \end{cases} \quad (44)$$

$$P_{NET} = P_{BAT} = P_{PV} + P_{WT} - P_{LOAD} - P_{LOSS} \quad (45)$$

where, P_{BAT} is battery bank power, when the loads are fed and P_{LOAD} is current demanded load power, P_{PV} and P_{WT} are generated power from PV array and wind turbine, respectively, P_{LOSS} is the total power loss in the system. The battery bank has 14400 Wh energy capacity with 100 % of *SoC* level, even if any DGs are ineffective to generate power, whole load group can be feed during 8.62 hours with a full capacity of battery bank in the battery mode on. The demanded net power (P_{NET}) can be defined as (45) according to the operation mode.

When a case study is performed to determine in simulation results as follows:

- Initially, the power is expected to become nearly the PV array of 1 kW, the wind turbine of 400 W, if the irradiance, temperature and wind speed are optimum to produce energy of course. These DGs are connected to the battery bank indirectly. The battery bank is directly connected to the loads through the bidirectional DC-DC buck-boost converter. Precisely, we can say that the DGs feed the battery bank. The power generated by the PV panels and the wind turbine is tried to hold close to the rated 1.4 kW by the MPPT control and is returned to the battery bank.
- For better illustration, we can handle a virtual lesson that is held in the aforementioned laboratory. At first, a lighting armature (520 W) is plugged in and consumes the battery bank connected to the PV and wind turbine system. At the same time, a power supply (600 W) is turned on. The same sequence is then reconnected for the next lesson. The remaining of the generated power from RESs is returned to charge the batteries.
- After these lessons, a multimeter (250 W) is plugged in to measure some variables on purpose in the lab. If the DGs do not supply sufficient power to the loads, therefore the battery bank is discharged until the desired safety SoC_{min} level. Otherwise, it is charged once the power is more satisfactory than load demand. Even if the battery bank is not sufficient to supply, the complementary power is provided by the utility grid after changing operation mode to feed the load groups and charge batteries.
- Before or after this utilization at any time, in case the *SoC* level is more than defined SoC_{max}, in order for the

This work is licensed under a Creative Commons Attribution 4.0 License. For more information, see https://creativecommons.org/licenses/by/4.0/

This article has been accepted for publication in a future issue of this journal, but has not been fully edited. Content may change prior to final publication. Citation information: DOI 10.1109/ACCESS.2021.3072899, IEEE Access

batteries not to overcharge, the electrolyser is switched on to generate H_2 and then store H_2 in the H_2 metal hydride tube for supplying to the fuel cell system. With the aim of filling the H_2 tube, the fuel cell system will be ready for operation.

The fuel cell which contains many complex structures attains the required operational drive from this microgrid with clean energy. The system has been proven to work smoothly with this case study with simulation and experimental results. This case study represents not only an empirical scenario but also a routine scenario during a laboratory lesson. Naturally, in this scenario, the utilization of the system, load groups, and control algorithms can be varied, the required innovations for educational research and development activities can be tried. As can be depicted in Fig. 9, this EMS generates various control signals based on the data it receives from DGs, loads and the grid. These signals control the power electronics converters, which are the main carriers of the system, and the relays for switching on-off the grid, loads, and converters.

It is worth mentioning that battery storage systems play a key role in improving the microgrid's stability and reducing the detrimental effects of the intermittent nature of the RESs. The primary power source to the loads is the PV array and wind turbine; however, the battery bank store surplus power generated from the PV side as complementary power sources. Once the PV array and wind turbine system cannot afford sufficient power (due to insufficient weather conditions) and also *SoC* of the battery bank is lower than the defined value (SoC_{min}), thus isolated operation ends, and the complementary power is provided by the grid.

V. SIMULATION RESULTS

Simulation and experimental results are revealed to verify the system with the proposed EMS requirements. As inputs of the DGs, solar irradiance, temperature, and wind speed are generated by obtaining a scaled dataset of a weather station for utilization in the simulation model. When being defined a random load pattern of a lesson that is held in the laboratory, it is possible that the power curve of these defined loads to see from Fig. 10. As can be shown in Fig. 10 (a), among t = 0.05 – 0.15 s and again t = 0.25 – 0.35 s, the lighting armature was got involved with its power beyond 500 W. During these times, the power supply was turned on as seen in Fig. 10 (b). After t = 0.45 s, the electrolyser was switched on with the power of 300 W to generate H_2 gas to fuel cell operation about 0.20 seconds. At this time, the multimeter demanded power for 0.20 s to measure some variables in the lesson, as can be seen in Fig. 10 (c) and (d). Thereby, all plug on-off moments belong to the loads can be shown in Fig. 10 separately. As a known argument that the frequency of the AC loads should correspond to the grid frequency such as 50 or 60 Hz, the operating frequency of the AC loads can be extracted from the period of their waveform existing in Fig. 11. As seen, the waveform periods are equal to each other and it is obvious that one period is 20 ms, so the frequency of the AC loads can be considered as 50 Hz.

The lighting armature and then power supply gets involved consecutively, so the observed step of the stair in the battery power could be ascribed to an increment of load demand. Similarly, the multimeter gets involved during the electrolysis operation, thus another lower step than the previous one can be stem from that other demand in Fig. 11 (b). There are three consecutive load demands as to why this result was observed. Additionally, from t = 0.9 s to the end, in the nonexistence of any load demands, an observed rise in Fig. 13 (c) could be attributed to a small drop of the battery bank power under the solar power effect as can be seen from Fig. 15 (b). The input profiles of the DGs such as solar and wind have been obtained from the weather station can be shown in Fig. 12 with the weather station's scaled data. These data can be assessed as the effect of variable profile in input to the system as seen in Fig. 13 (a) and (b).

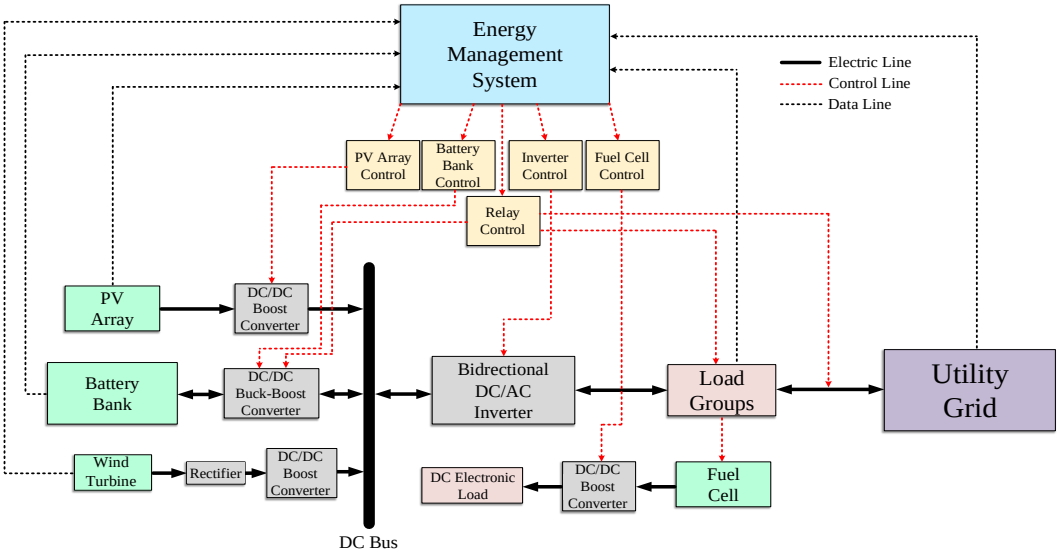

FIGURE 9. **The general block diagram of the discussed system.**

This work is licensed under a Creative Commons Attribution 4.0 License. For more information, see https://creativecommons.org/licenses/by/4.0/

This article has been accepted for publication in a future issue of this journal, but has not been fully edited. Content may change prior to final publication. Citation information: DOI 10.1109/ACCESS.2021.3072899, IEEE Access

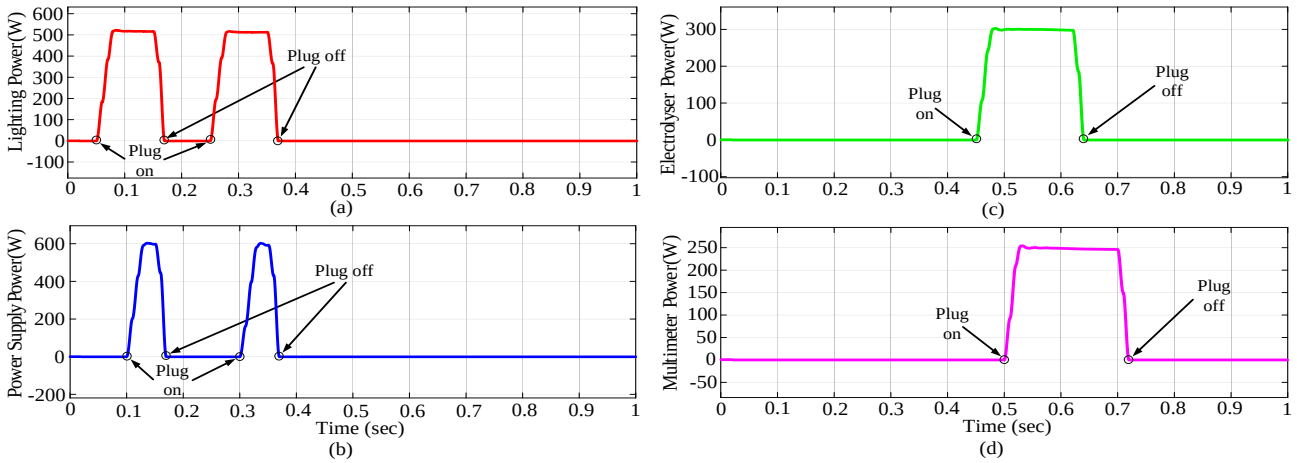

FIGURE 10. **The curves of the load powers: (a) Lighting power, (b) power supply power, (c) electrolyser power and lastly (d) multimeter power.**

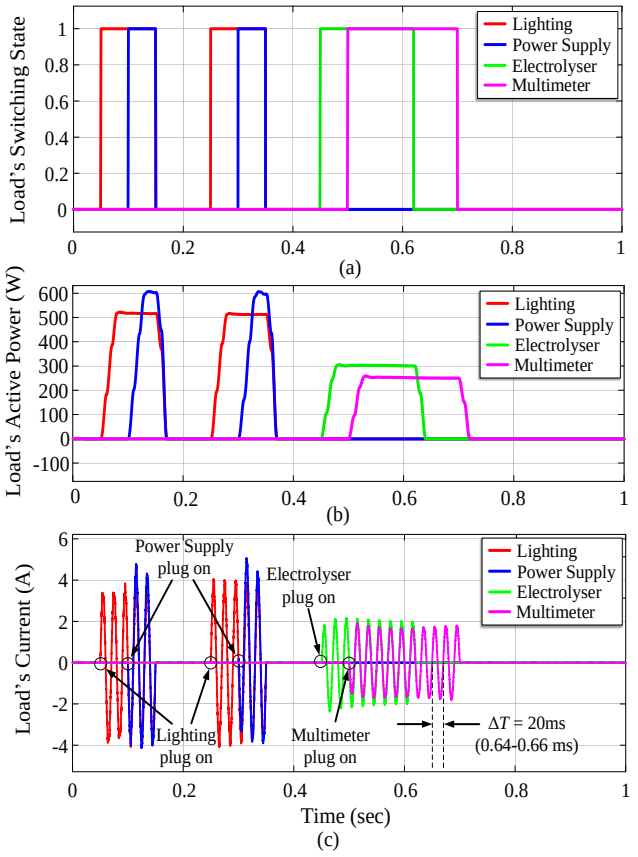

FIGURE 11. **The curves of loads: (a) Load's switching state, (b) load's active powers and (c) load's current.**

Steady-state of the fuel cell in the presence of the fuel as seen in Fig. 14 (a), takes about 5 seconds. The air and fuel flow rates resemble a parallel characteristic to the generated power, but the stack efficiency is inversely related to the generated power as seen in Fig. 14 (b) and (c). As a result of the case study defined in the simulation, electrolyser has stopped t = 0.64 s. Electrolyser has stored hydrogen for the fuel cell utilization during this operating time. According to energy management algorithms at t = 0.7 s the fuel cell has absorbed the stored fuel to generate power with the help of continuous operation of the flow rate regulator.

For better illustration of the case study, it is obvious to see at first glance to Fig. 15 is divided into twelve events. To this end, the analyzing of the system behavior gets easy well. Actually, Fig. 15 depicts the behavior of the main power supply i.e., the battery bank. Fig. 15 (a) shows the *SoC* level of the battery bank, which indicates the percentage value related to its capacity, also provides to make battery intelligible to the people. Within this scope, Fig. 15 (b), (c) and (d) show the battery bank power, current, and voltage respectively. Before proceeding, it is important to refer that the shape of the current curve is the same as the power curve, unlike the voltage curve. When the current is positive, that means discharging, otherwise corresponds charging. These divided events can be aligned as follows.

The first, eleventh, and twelfth event show that no loads are getting involved and the battery bank is charged with a 500 W power. In the second event, the lighting is approximately 500 W, which is activated. Thus, the *SoC* level remains constant during this time. Once the other load is activated for the third event, the batteries are discharged and the *SoC* level decreases.



FIGURE 12. **Weather station on the rooftop of laboratory building for meteorological data utilization.**

This work is licensed under a Creative Commons Attribution 4.0 License. For more information, see https://creativecommons.org/licenses/by/4.0/

This article has been accepted for publication in a future issue of this journal, but has not been fully edited. Content may change prior to final publication. Citation information: DOI 10.1109/ACCESS.2021.3072899, IEEE Access

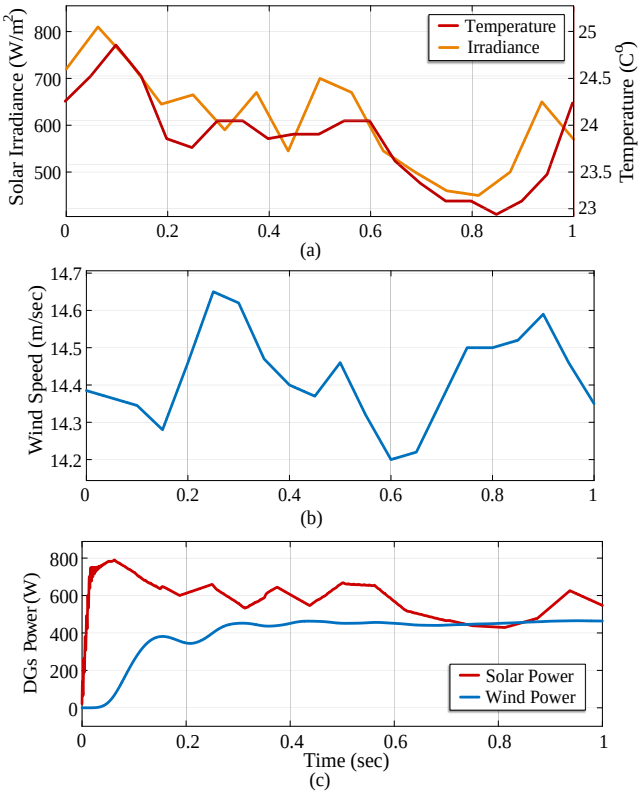

FIGURE 13. **The input profiles: (a) solar irradiance and temperature, (b) wind speed and (c) distributed generations power.**

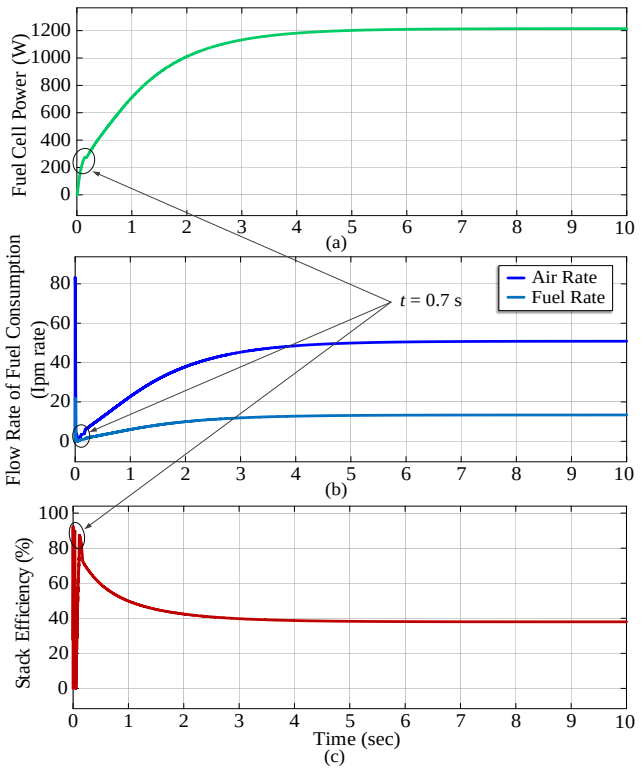

FIGURE 14. **The operation outputs of the fuel cell system during 10 seconds; (a) the power of the fuel cell, (b) flow rate of fuel consumption in terms of insertion paddlewheel meter (lpm), and (c) stack efficiency of the fuel cell system.**

For the fourth event, since there is no load up to t = 0.25 s, the batteries are fed by the DGs within their capacity as shown in Fig. 15 (c), the current is negative and the batteries are charged. In the fifth and sixth event, the lighting armatures and the power supply are again activated in sequence and act quite similar characteristic close to the second and third events. However, the reason for this is not the same because the power provided by the DGs in this pattern is less than the power of the second and third events, so the *SoC* level tends to fall.

The seventh event is similar to the fourth event, but the rising slope of the *SoC* level is slightly less due to the existing lower power of the DGs. In the eighth event, with the inclusion of less load power i.e., electrolyser in the no-load profile, the power from the DGs is compensated slightly, is decreased the slope of the rise of the *SoC* but its level has been rising. After that case, the multimeter is switched on at the ninth event, the loads drain the battery slightly. With the multimeter is switched off and the power of the DGs in the tenth event, the batteries are recharged to a small extent. Lastly, as the eleventh and twelfth events have similarly unloaded profiles, so the DGs power are transferred and charged to the batteries. In the twelfth event, the higher charging slope is due to the higher power of the DGs.

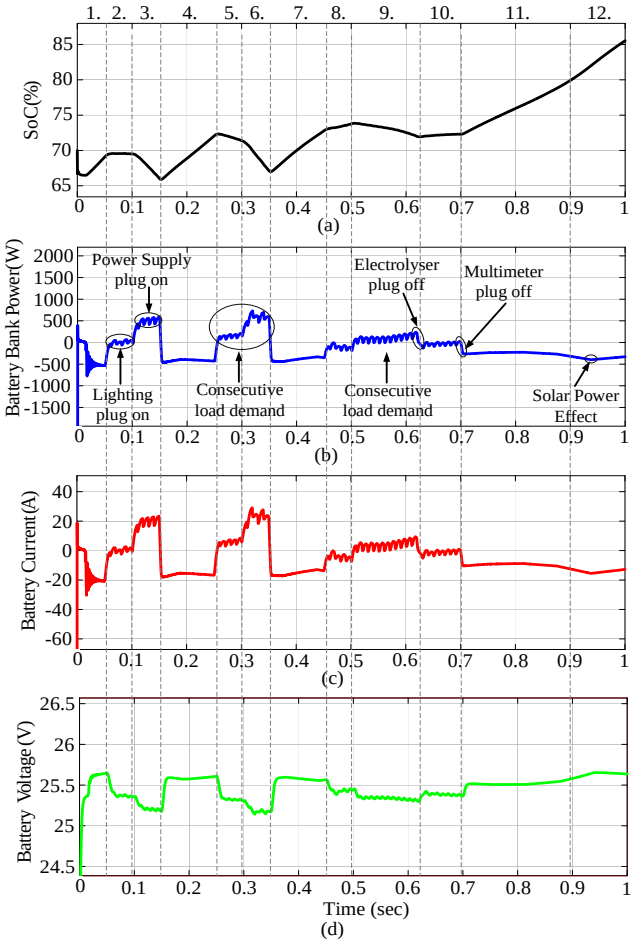

FIGURE 15. **The curves of battery bank, (a) *SoC* level, (b) power, (c) current, and (d) voltage.**

This work is licensed under a Creative Commons Attribution 4.0 License. For more information, see https://creativecommons.org/licenses/by/4.0/

This article has been accepted for publication in a future issue of this journal, but has not been fully edited. Content may change prior to final publication. Citation information: DOI 10.1109/ACCESS.2021.3072899, IEEE Access

VI. REAL TIME OPERATION WITH EXPERIMENTAL RESULTS

Experimental results are carried out to support the simulation results. Initially, the modeled high penetration RES laboratory-scale microgrid has been installed. Then, a real-time test system has been created for the operation with control and proposed energy management algorithm. The EMS has been designed and oriented with the help of an interface of management software for the DC-AC interlinking inverter named '*WatchPower*©' connected to the computer and all hardware. As can be shown in Fig. 16 shows all the components of the mentioned system. The PV array and wind turbine are located on the roof of the building in which the laboratory exists. The fuel cell, power converters, and AC load groups exist inside the laboratory.

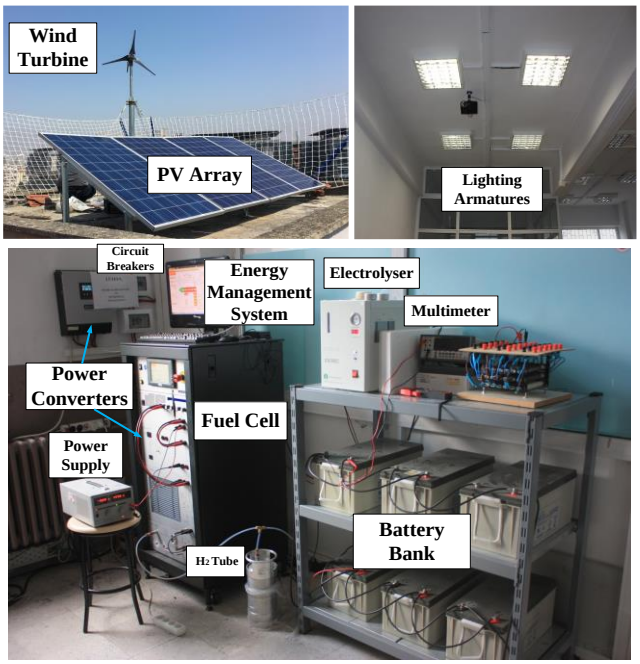

FIGURE 16. Experimental setup of laboratory scale microgrid system.

To gather experimental data under the same load-pattern order and see whether the proposed EMS satisfies the AC loads or not, the system has been run for 30 minutes with two different EMS cases. Afterwards, the experimental data were collected per half minute, analyzed, plotted, and compared with the simulation results.

In a similar way, the AC loads are got involved in the same order likewise the simulation. Firstly, the time when between t = 1.5 – 4.5 min and t = 7.5 – 10.5 min the lighting armatures are operated. At the last 1.5 minutes of these time intervals, the power supply is run, consecutively. The electrolyser is got involved in the system between t = 13.5 – 18.6 min. At this operation time, the multimeter is plugged-on for 6 minutes until t = 21 min.

As stated previously, the data acquisition interface namely, WatchPower© enables users to define beginning conditions in advance for the system operation. Two different EMS cases have been defined by being changed the output source priority as 1) *solar* and 2) *SBU* (i.e., solar-battery-utility grid) properties with aim of targeting the charger source priority as only II) *solar-first*. The experimental results have been tried to obtain by close input and output (load) conditions as far as possible. The combination of cases has been operated as follows:

i. 1) *Solar* and II) *solar-first* couple, while the average solar irradiance has been obtained 849 W/m^2, the average wind speed has been 12.4 m/sec for *Case 1*.
ii. After 10 minutes later, *Case 2* has been identified to the system. The average solar irradiance has been measured as 812 W/m^2 and the wind speed has been 13.2 m/sec with 2) *SBU* and II) *solar-first* couple.

With experimental data acquisition during these cases, active load power, battery power, and DGs power (the actual power DGs i.e., P_{DGs}=P_{PV}+P_{WT}) are shown in Fig. 17. It is useful to mention that once the experimental data was gathering, wind speed was pretty low. Regarding battery bank, *SoC* level, power, current and voltage curves can be shown in Fig. 18. With a fast drop of the DGs power, the batteries discharge to supply the loads. The real losses in the system can be also calculated as (45).

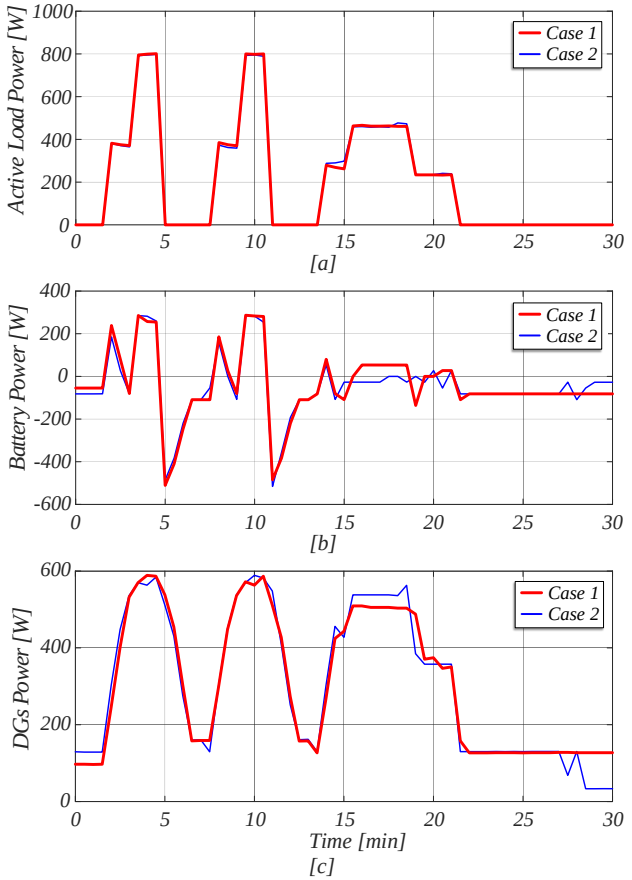

FIGURE 17. Experimental data curves; (a) active load power, (b) battery bank power, and (c) demanded DGs power (sum of PV and WT power).

Two different cases are tested on the laboratory-scale microgrid for further performance validation. As *Case 1* includes the output source priority as 1) *solar*, the main power sources performs a bit smoother operation without

This work is licensed under a Creative Commons Attribution 4.0 License. For more information, see https://creativecommons.org/licenses/by/4.0/

This article has been accepted for publication in a future issue of this journal, but has not been fully edited. Content may change prior to final publication. Citation information: DOI 10.1109/ACCESS.2021.3072899, IEEE Access

unnecessary peaks when compared to *Case 2*. Moreover, it is obvious that the experimental results have similar results to the simulation results which are compared to each other. It can be considered explicitly that dispatching surplus power is to store the battery bank. Due to the natural behavior Battery bank current and power have a parallel characteristic curve, unlike the voltage is opposite. With the energy management algorithm, the system puts the microgrid into grid mode without falling under the SoC_{min} level to operate the battery bank in a healthy band.

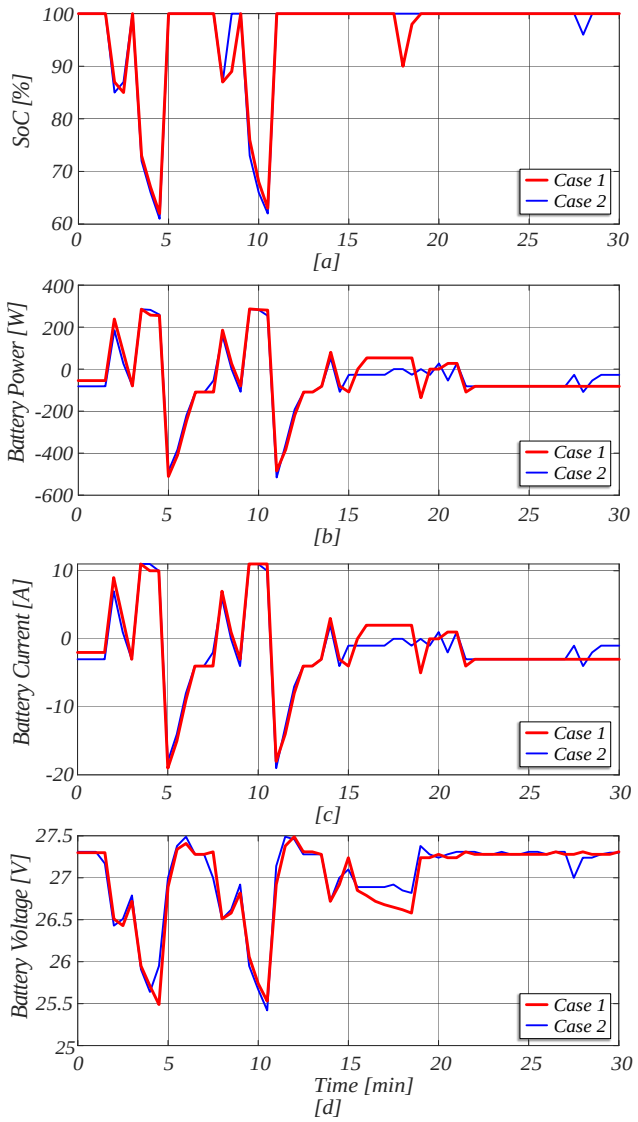

FIGURE 18. **Experimental data curves regarding battery bank; (a) *SoC* level, (b) power, (c) current and lastly (d) voltage.**

In grid mode, the system feeds the loads in case of any demands and also charges the batteries once no loads exist. In other words, the loads are supplied by the grid in this mode, so the batteries are supplied by the power obtained from the DGs (if still exists) or by the grid.

With the aim of verifying the system operation, another scenario was implemented by defining the initial SoC_{min} and SoC_{max} value as 60% and 80%, respectively.

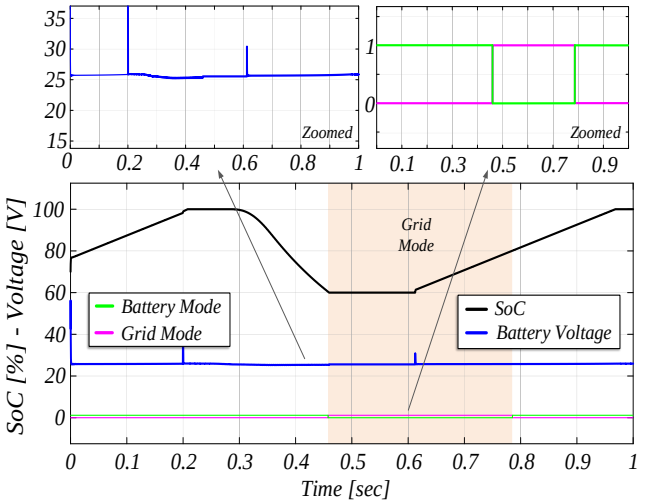

FIGURE 19. **Simulation results of multi-mode operation with an initial 70% *SoC*. Between nearly *t*=0.45~0.78 s, the system was operated in grid mode. Due to lack of any load *t*=0.61 s the batteries were fed.**

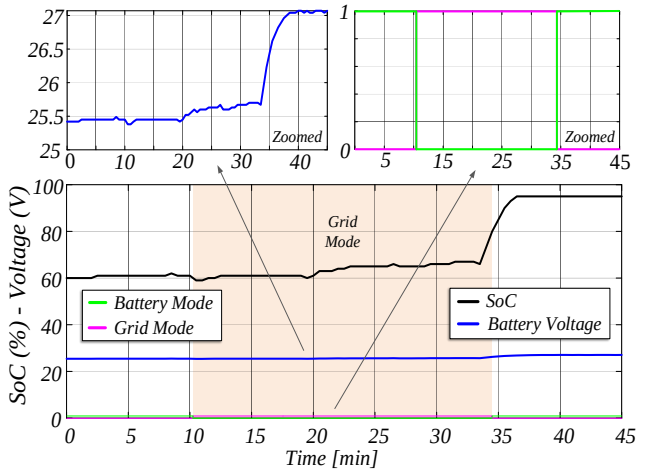

FIGURE 20. **Experimental results of multi-mode operation with *Case 1* with an initial 60% *SoC*. At *t*=10.29 min the loads were fed with grid mode and then nearly at *t*=34.5 min, the battery mode was ON again.**

When the battery capacity decreased lower 60%, the system switches to the grid mode and continues to feed the loads through the utility grid. The battery capacity can only be integrated into the system by switching back to battery mode after having a reasonable *SoC* level of 80%. Thereby, Fig. 19 represents the simulation result of this multi-mode operation scenario and also Fig. 20 refers to the experimental result of this scenario. As a result, we can assert that the main sources of the load demand-side management of the system are DGs, batteries, and lastly the utility grid respectively.

VII. CONCLUSION

In this paper, design implementation, modeling, and operation of a standalone microgrid have been proposed for a laboratory-scale education and research laboratory experimental microgrid. In comparison with the unstable character of RESs, continuous and reliable power has been tried to achieve and provide from the DGs to the loads. The

This work is licensed under a Creative Commons Attribution 4.0 License. For more information, see https://creativecommons.org/licenses/by/4.0/

This article has been accepted for publication in a future issue of this journal, but has not been fully edited. Content may change prior to final publication. Citation information: DOI 10.1109/ACCESS.2021.3072899, IEEE Access

experimental setup has been performed smoothly, whose results have complementary behavior as the simulation results are striking. Although the fluctuation of the DGs input exists, the battery bank could smooth harmonics, satisfy the AC loads thanks to the neat control and operation of the power converters. Once more than one load is included in the load group at the same time, the system meets these loads without overshoots. The proposed EMS cases have been implemented to protect battery lifetime and also succeeded in the assigned operations to improve flexibility for the general system. Thus, it can be extracted from the experimental results that the peak power and fluctuation are relatively diminished successfully. The system has been proven to work smoothly with this case study with simulation and experimental results.

The proper model, robust installation, and healthy operation of this laboratory-scale microgrid provides a ready basis for more sophisticated researches in the future. Moreover, the system can be proposed for residential applications, particularly which have critical loads to provide continuous power flow with the help of a desired EMS. In this laboratory-scale microgrid, all the system need is supplied via green energy during a lesson, which is noteworthy and instructive. The studied system improves the quality of education and research, under multiple disciplines in electrical engineering. Notably, this system structure has presented the possibility of studying in many fields such as renewables, control, power electronics, software, etc. to researchers and students.

REFERENCES

[1] A. N. Akpolat and E. Dursun, "From Microgrid to Smart Grid: A Review of Campus Projects," in *International Engineering, Science and Education Conference*, Diyarbakir, Turkey, Dec. 2016, pp. 379-387.

[2] E. Unamuno and J. A. Barrena, "Hybrid ac/dc microgrids - Part I: Review and classification of topologies," *Renew. Sust. Energ. Rev.*, vol. 52, pp.1251-1259, Dec. 2015.

[3] B. Benlahbib, N. Bouarroudj, S. Mekhilef, D. Abdeldjalil, T. Abdelkrim, F. Bouchafaa, and A. lakhdari, "Experimental investigation of power management and control of a PV/wind/fuel cell/battery hybrid energy system microgrid," *Int. J. Hydrogen Energy*, vol. 45, no. 53, pp. 29110-29122, Oct. 2020.

[4] A. N. Akpolat, *et al*., "Sensorless Control of DC Microgrid Based on Artificial Intelligence," *IEEE Trans. Energy Convers.*, Early Access, Dec. 2020, doi: 10.1109/TEC.2020.3044270.

[5] M. Davari and Y. A. I. Mohamed, "Robust Droop and DC-Bus Voltage Control for Effective Stabilization and Power Sharing in VSC Multiterminal DC Grids," *IEEE Trans. Power Electron.*, vol. 33, no. 5, pp. 4373-4395, May 2018.

[6] N. Eghtedarpour and E. Farjah, "Power control and management in a Hybrid AC/DC microgrid," *IEEE Trans. Smart Grid*, vol. 5, no. 3, pp. 1494-1505, May. 2014.

[7] N. R. Tummuru, U. Manandhar, A. Ukil, H. B. Gooi, S. K. Kollimalla, and S. Naidu, "Control strategy for AC-DC microgrid with hybrid energy storage under different operating modes," *Int. J. Electr. Power Energy Syst.*, vol. 104, pp. 807-816, Jan. 2019.

[8] B. R. Naidu, G. Panda and P. Siano, "A Self-Reliant DC Microgrid: Sizing, Control, Adaptive Dynamic Power Management, and Experimental Analysis," *IEEE Trans. Ind. Informat.*, vol. 14, no. 8, pp. 3300-3313, Aug. 2018.

[9] A. Gupta, S. Doolla, and K. Chatterjee, "Hybrid AC–DC Microgrid: Systematic Evaluation of Control Strategies," *IEEE Trans. Smart Grid*, vol. 9, no. 4, pp. 3830-3843, Jul. 2018.

[10] B. Ko, G. Lee, K. Choi, and R. Kim, "A Coordinated Droop Control Method Using a Virtual Voltage Axis for Power Management and Voltage Restoration of DC Microgrids," *IEEE Trans. Ind. Electron.*, vol. 66, no. 11, pp. 9076-9085, Nov. 2019.

[11] X. Li, D. Hui, L. Wu, and X. Lai, "Control strategy of battery state of charge for wind/battery hybrid power system," in *Proc. 2010 IEEE International Symposium on Industrial Electronics*, Bari, Italy, Jul. 2010, pp. 2723-2726.

[12] J. Hu, Y. Xu, K. W. Cheng, and J. M. Guerrero, "A model predictive control strategy of PV-Battery microgrid under variable power generations and load conditions," *Appl. Energy*, vol. 221, pp. 195-203, Jul. 2018.

[13] T. A. Kattakayam and K. Srinivasan, "Lead acid batteries in solar refrigeration systems," *Renew. Energy*, vol. 29, no. 8, pp. 1243-1250, Jul. 2004.

[14] M. Eroglu, G. Kepoglu, S. Sevencan, S. Yazici, E. Dursun, and J. Song, "A Stand-alone Mobile House Using PV/Wind/Fuel Cell Hybrid Power System," in *Proc. 3rd World Congress of Young Scientists on Hydrogen Energy Systems*, Oct. 2009.

[15] E. Wikner and T. Thiringer, "Extending battery lifetime by avoiding high SOC," *Appl. Sci.*, vol. 8, no. 10, pp.1825, Oct. 2018.

[16] M. Castañeda, A. Cano, F. Jurado, H. Sanchez, and L. M. Fernandez, "Sizing optimization, dynamic modeling and energy management strategies of a stand-alone PV/hydrogen/battery-based hybrid system," *Int. J. Hydrogen Energy*, vol. 38, no. 10, pp. 3830-3845, Apr. 2013.

[17] E. Ipek, M. K. Eren, and M. Yilmaz, "State-of-Charge Estimation of Li-ion Battery Cell using Support Vector Regression and Gradient Boosting Techniques," in *Proc. 2019 International Aegean Conference on Electrical Machines and Power Electronics (ACEMP) & 2019 International Conference on Optimization of Electrical and Electronic Equipment (OPTIM)*, Istanbul, Turkey, Aug. 2019, pp. 604-609.

[18] M. Lei, *et. al.* "An MPC-Based ESS Control Method for PV Power Smoothing Applications," *IEEE Trans. Power Electron.*, vol. 33, no. 3, pp. 2136-2144, Mar. 2018.

[19] H. Rahimi-Eichi, F. Baronti, and M. Y. Chow, "Modeling and online parameter identification of Li-Polymer battery cells for SOC estimation," in *Proc. IEEE International Symposium on Industrial Electronics*, Hangzhou, China, 2012, pp. 1336-1341.

[20] L. Wang, L. Wang, and C. Liao, "Research on Improved EKF Algorithm Applied on Estimate EV Battery SOC," in *Proc. 2010 Asia-Pacific Power and Energy Engineering Conference*, Chengdu, China, 2010, pp. 1-4.

[21] W. Waag, C. Fleischer, and D. U. Sauer, "Critical review of the methods for monitoring of lithium-ion batteries in electric and hybrid vehicles," *J. of Power Sources*, vol. 258, pp. 321-339, Jul. 2014.

[22] Z. Roumila, D. Rekioua, and T. Rekioua, "Energy management based fuzzy logic controller of hybrid system wind/photovoltaic/diesel with storage battery', *Int. J. Hydrogen Energy*, vol. 42, no. 30, pp. 19525-19535, Jul. 2017.

[23] J. P. Torreglosa, P. García, L. M. Fernández, and F. Jurado, "Energy dispatching based on predictive controller of an off-grid wind turbine/photovoltaic/hydrogen/battery hybrid system," *Renew. Energy*, vol. 74, pp. 326-336, Feb. 2015.

[24] E. H. Trinklein, G. G. Parker, R. D. Robinett, and W. W. Weaver "Toward Online Optimal Power Flow of a Networked DC Microgrid System," *IEEE Trans. Emerg. Sel. Topics Power Electron.*, vol. 5, no. 3, pp. 949-959, Sep. 2017.

[25] M. A. Hossain, H. R. Pota, S. Squartini, et. al.: 'Energy management of community microgrids considering degradation cost of battery', *J. Energy Storage*, vol. 22, pp. 257-269, Apr. 2019.

[26] M. F. Zia, M. Nasir, E. Elbouchikhi, M. Benbouzid, J. C. Vasquez, and J. M. Guerrero, "Energy Management System for an Islanded Renewables-based DC Microgrid," in *Proc. 2020 2nd International Conference on Smart Power & Internet Energy Systems (SPIES)*, Bangkok, Thailand, 2020, pp. 543-547.

[27] L. Xu and D. Chen, "Control and Operation of a DC Microgrid With Variable Generation and Energy Storage," *IEEE Trans. Power Del.*, vol. 26, no. 4, pp. 2513-2522, Oct. 2011.

This work is licensed under a Creative Commons Attribution 4.0 License. For more information, see https://creativecommons.org/licenses/by/4.0/

This article has been accepted for publication in a future issue of this journal, but has not been fully edited. Content may change prior to final publication. Citation information: DOI 10.1109/ACCESS.2021.3072899, IEEE Access

[28] A. Merabet, K. Tawfique Ahmed, H. Ibrahim, R. Beguenane and A. M. Y. M. Ghias, "Energy Management and Control System for Laboratory Scale Microgrid Based Wind-PV-Battery," *IEEE Trans. Sustain. Energy*, vol. 8, no. 1, pp. 145-154, Jan. 2017.

[29] N. Saxena, I. Hussain, B. Singh, and A. L. Vyas, "Implementation of a Grid-Integrated PV-Battery System for Residential and Electrical Vehicle Applications," *IEEE Trans. Ind. Electron.*, vol. 65, no. 8, pp. 6592-6601, Aug. 2018.

[30] L. Guo, *et. al.*, "Energy Management System for Stand-Alone Wind-Powered-Desalination Microgrid," *IEEE Trans. Smart Grid*, vol. 7, no. 2, pp. 1079-1087, Mar. 2016.

[31] D. A. Sbordone, K. M. M. Huq, and M. Baran, "An experimental microgrid for laboratory activities," in *Proc. 2015 IEEE 15th International Conference on Environment and Electrical Engineering (EEEIC)*, Rome, Italy, Jun. 2015, pp. 363-367.

[32] A. A. Jabbar, A. Y. Elrayyah, M. Z. C. Wanik, A. P. Sanfilippo, and N. K. Singh, "Development of Hybrid AC/DC Laboratory-scale Smart Microgrid Testbed with Control & Monitoring System Implementation in LabVIEW," in *Proc. 2019 IEEE PES GTD Grand International Conference and Exposition Asia (GTD Asia)*, Bangkok, Thailand, Mar. 2019, pp. 889-894.

[33] N. S. Coleman, K. L. Ogawa, J. Hill, and K. N. Miu, "Reconfigurable Distribution Automation and Control Laboratory: Solar Microgrid Experiments," *IEEE Trans. Power Syst.*, vol. 33, no. 6, pp. 6379-6386, Apr. 2018.

[34] J. J. G. Rojas, D. A. Z. Prada, and W. A. L. M. O. Lopez-Santos, "Real-Time Small-Scale Wind Turbine Emulator for a Hybrid Microgrid Laboratory Testbed," in *Proc. 2019 IEEE Workshop on Power Electronics and Power Quality Applications (PEPQA)*, Manizales, Colombia, May 2019, pp. 1-6.

[35] A. N. Akpolat, Y. Yang, F. Blaabjerg, E. Dursun, and A. E. Kuzucuoğlu, "Modeling Photovoltaic String in PLECS Under Partial Shading," in *Proc. 2019 International Conference on Power Generation Systems and Renewable Energy Technologies (PGSRET)*, Istanbul, Turkey, Aug. 2019, pp. 1-6.

[36] H. S. Sahu, S. Kumar and S. K. Nayak, "Maximum Power Point Estimation of a PV Array by Using Improve Bisection Method," in 2018 IEEE Transportation Electrification Conference and Expo, Asia-Pacific (ITEC Asia-Pacific), Bangkok, Jun. 2018, pp. 1-5.

[37] Y. Ma, H. Wen and X. Li, "A Novel Photovoltaic String Model Based on the Lambert w Function for Partial Shading Conditions," *in Proc. 2018 IEEE International Conference on Power Electronics, Drives and Energy Systems (PEDES)*, Chennai, India, Dec. 2018, pp. 1-6.

[38] D. Sera, L. Mathe, T. Kerekes, S. V. Spataru, and R. Teodorescu, "On the Perturb-and-Observe and Incremental Conductance MPPT Methods for PV Systems," *IEEE J. of Photovolt*., vol. 3, no. 3, pp. 1070-1078, May 2013.

[39] Z. Chen, "Wind turbine drive train systems," in *Wind Energy Systems: Optimising Design and Construction for Safe and Reliable Operation*, 1st ed., UK: Woodhead Publishing Limited, 2011, pp. 206-246.

[40] O. C. Onar and A. Khaligh, "Alternative Energy in Power Electronics," in *Chapter 2-Energy Sources*, 1st ed., UK: Butterworth-Heinemann, Elsevier, 2015, pp. 81-154.

[41] A. Bouscayrol, P. Delarue, and X. Guillaud, "Power strategies for maximum control structure of a wind energy conversion system with a synchronous machine," *Renew. Energy*, vol. 30, no. 15, pp. 2273-2288, Dec. 2005.

[42] S. Heier, "Wind Energy Conversion System," in *Grid Integration of Wind Energy: Onshore and Offshore Conversion Systems*, 3rd ed., Germany: John Wiley & Sons, 2014, pp. 31-117.

[43] S. F. Fux, M. J. Benz, and L. Guzzella, "Economic and environmental aspects of the component sizing for a stand-alone building energy system: A case study," *Renew. Energy*, vol. 55, pp.438-447, Jul. 2013.

[44] A. Nabi Akpolat, Y. Yang, F. Blaabjerg, E. Dursun, and A. Emin Kuzucuoğlu, "Li-ion-based Battery Pack Designing and Sizing for Electric Vehicles under Different Road Conditions," in *Proc. 2020 International Conference on Smart Energy Systems and Technologies (SEST)*, Istanbul, Turkey, Sep. 2020, pp. 1-6,

[45] O. Tremblay, L.A. Dessaint, "Experimental Validation of a Battery Dynamic Model for EV Applications," *World Electr. Veh. J.*, vol. 3, no. 2, pp. 289-298, Jun. 2009.

[46] Z. U. Bayrak and M. T. Gencoglu, "Simulation and experimental study of a hybrid system for different loads," in *Proc. 2014 International Conference on Renewable Energy Research and Application (ICRERA)*, Milwaukee, WI, Oct. 2014, pp. 451-456.

[47] K. Xin and A. M. Khambadkone, "Dynamic modelling of fuel cell with power electronic current and performance analysis," in *Proc. The Fifth International Conference on Power Electronics and Drive Systems, 2003. PEDS 2003.*, Singapore, Nov. 2003, pp. 607-612.

[48] J. Larminie and A. Dicks, "Operational Fuel Cell Voltages" in *Fuel Cell Systems Explained*, 2nd ed., UK: John Wiley & Sons, 2003, pp.45-66.

[49] S. Njoya M. O, Tremblay, and L. Dessaint, "A generic fuel cell model for the simulation of fuel cell vehicles," *in Proc. 2009 IEEE Vehicle Power and Propulsion Conference*, Dearborn, MI, Sep. 2009, pp. 1722-1729.

[50] R. O'Hayre, S.-W. Cha, W. Colella, and F. B. Prinz, "Fuel Cell Principles" in *Fuel Cell Fundamentals*, 3rd ed., USA: Wiley & Sons, 2016, pp. 3-24.

[51] E. Koutroulis, Y. Yang, and F. Blaabjerg, "Co-Design of the PV Array and DC/AC Inverter for Maximizing the Energy Production in Grid-Connected Applications," *IEEE Trans. Energy Convers.*, vol. 34, no. 1, pp. 509-519, Mar. 2019.

[52] M. Dursun and M. K. Döşoğlu, "LCL Filter Design for Grid Connected Three-Phase Inverter," in *Proc. 2018 2nd International Symposium on Multidisciplinary Studies and Innovative Technologies (ISMSIT)*, Ankara, Oct. 2018, pp. 1-4.

[53] S. Golestan and J. M. Guerrero, "Conventional synchronous reference frame phase-locked loop is an adaptive complex filter," *IEEE Trans. Ind. Electron.*, vol. 62, no. 3, pp. 1679–1682, Mar. 2015.



ALPER NABI AKPOLAT (S'19) received the B.Sc. degree in Electrical-Electronics Engineering and the M.Sc. degree in Mechatronics Engineering from Firat University, Elazig, Turkey, in 2012 and 2015, respectively. He is currently working toward the Ph.D. degree in Electrical-Electronics Engineering and also serving as a Research Assistant, from Faculty of Technology, at Marmara University, Istanbul, Turkey.

From March 2019, he has been a Guest Ph.D. student during one year with Department of Energy Technology, Aalborg University, Denmark. His research interests include renewable energy systems, DC microgrids, applied artificial intelligence in power electronics and power systems, and control of distributed generation systems.



YONGHENG YANG (SM'17) received the B.Eng. degree in Electrical Engineering and Automation from Northwestern Polytechnical University, China, in 2009 and the Ph.D. degree in Energy Technology from Aalborg University, Denmark, in 2014. He was a postgraduate student with Southeast University, China, from 2009 to 2011. In 2013, he spent three months as a Visiting Scholar at Texas A&M University, USA. Since 2014, he has been with the Department of Energy Technology, Aalborg University, where he became a tenured Associate Professor in 2018. In January 2021, he joined Zhejiang University, China, where he is now a ZJU100 Young Professor at the Department of Electrical Engineering.

Dr. Yang was the Chair of the IEEE Denmark Section (2019-2020). He is the secretary for the Technical Committee of Sustainable Energy Systems (TC5) of the IEEE PELS. He is an Associate Editor for several IEEE Transactions/Journals and a Deputy Editor of the *IET Renewable Power Generation* for Solar Photovoltaic Systems. He received the 2018

This work is licensed under a Creative Commons Attribution 4.0 License. For more information, see https://creativecommons.org/licenses/by/4.0/

This article has been accepted for publication in a future issue of this journal, but has not been fully edited. Content may change prior to final publication. Citation information: DOI 10.1109/ACCESS.2021.3072899, IEEE Access

IET Renewable Power Generation Premium Award and was an Outstanding Reviewer for the IEEE TRANSACTIONS ON POWER ELECTRONICS in 2018. In addition, he has received two IEEE Best Paper Awards. His current research is to tackle the issues brought by the integration of photovoltaic systems and multi-energy vectors through developing reliable and efficient power converters with advanced control.



FREDE BLAABJERG (S'86–M'88–SM'97–F'03) was with ABB-Scandia, Randers, Denmark, from 1987 to 1988. From 1988 to 1992, he got the PhD degree in Electrical Engineering at Aalborg University in 1995. He became an Assistant Professor in 1992, an Associate Professor in 1996, and a Full Professor of power electronics and drives in 1998. From 2017 he became a Villum Investigator. He is honoris causa at University Politehnica Timisoara (UPT), Romania and Tallinn Technical University (TTU) in Estonia.

His current research interests include power electronics and its applications such as in wind turbines, PV systems, reliability, harmonics and adjustable speed drives. He has published more than 600 journal papers in the fields of power electronics and its applications. He is the co-author of four monographs and editor of ten books in power electronics and its applications.

He has received 33 IEEE Prize Paper Awards, the IEEE PELS Distinguished Service Award in 2009, the EPE-PEMC Council Award in 2010, the IEEE William E. Newell Power Electronics Award 2014, the Villum Kann Rasmussen Research Award 2014, the Global Energy Prize in 2019 and the 2020 IEEE Edison Medal. He was the Editor-in-Chief of the IEEE TRANSACTIONS ON POWER ELECTRONICS from 2006 to 2012. He has been Distinguished Lecturer for the IEEE Power Electronics Society from 2005 to 2007 and for the IEEE Industry Applications Society from 2010 to 2011 as well as 2017 to 2018. In 2019-2020 he served as a President of IEEE Power Electronics Society. He has been Vice-President of the Danish Academy of Technical Sciences. He is nominated in 2014-2020 by Thomson Reuters to be between the most 250 cited researchers in Engineering in the world.



ERKAN DURSUN (S'05-M'13) received the B.Sc. degree (2001), the M.Sc. degree (2006), and Ph.D. degree (2013) in Electric Education, Faculty of Technical Education from Marmara University in Istanbul, Turkey. From 2010 to 2012, he was visiting fellow UNIDO-ICHET (United Nations Industrial Development Organization - International Centre for Hydrogen Energy Technologies).

From 2012 to 2013, he was a researcher with the Joint Research Center, European Commission, Italy. His research interest includes distributed generation, hybrid power systems, and smart grid. Dr. Dursun has been a member of IEEE for years, and also his papers have received more than 520 citations in SCI database of Thomson Reuters.



AHMET EMIN KUZUCUOĞLU (M'99) is an Associate Professor at Marmara University, Turkey. He received his B.Sc. degree from Electronics and Telecommunication Engineering Department, Istanbul Technical University, Turkey, in 1985 and he received his M.Sc. and Ph.D. degrees from Marmara University, in 1994 and 2000, respectively. He has been in England and the United States of America in 1987 as part of YÖK-World Bank Vocational School Project. He has been in Lithuania in July-2006 as part of EU Leonardo da Vinci Type A mobility project.

He is an Associate Professor with the Department of Electrical-Electronics Engineering. Since 2017, Dr. Kuzucuoğlu also currently serves as a Vice Dean of the Faculty of Technology at Marmara University, Istanbul, Turkey. He is an Editor-in-Chief of International Periodical of Recent Technologies in Applied Engineering (PORTA). His current research interests include industrial automation, robotics, AI, control theory and applications.

This work is licensed under a Creative Commons Attribution 4.0 License. For more information, see https://creativecommons.org/licenses/by/4.0/